Resolution of Maximum Entropy Method-Derived Posterior Conformational Ensembles of a Flexible System Probed by FRET and Molecular Dynamics Simulations

Jonas Dittrich,[∇] Milana Popara,[∇] Jakub Kubiak, Mykola Dimura, Bastian Schepers, Neha Verma, Birte Schmitz, Peter Dollinger, Filip Kovacic, Karl-Erich Jaeger,* Claus A. M. Seidel,* Thomas-Otavio Peulen,* and Holger Gohlke*

Read Online

ACCESS | Metrics & More | Article Recommendations | Supporting Information

ABSTRACT: Maximum entropy methods (MEMs) determine posterior distributions by combining experimental data with prior information. MEMs are frequently used to reconstruct conformational ensembles of molecular systems for experimental information and initial molecular ensembles. We performed time-resolved Förster resonance energy transfer (FRET) experiments to probe the interdye distance distributions of the lipase-specific foldase Lif in the *apo* state, which likely has highly flexible, disordered, and/or ordered structural elements. Distance distributions estimated from ensembles of molecular dynamics (MD) simulations serve as prior information, and FRET experiments, analyzed within a Bayesian framework to recover distance distributions, are used for optimization. We tested priors obtained by MD with different force fields (FFs) tailored to ordered (FF99SB, FF14SB, and FF19SB) and disordered proteins (IDPSFF and FF99SBdisp). We obtained five substantially different posterior ensembles. As in our FRET experiments the noise is characterized by photon counting statistics, for a validated dye model, MEM can quantify consistencies between experiment and prior or posterior ensembles. However, posterior populations of conformations are uncorrelated to structural similarities for individual structures selected from different prior ensembles. Therefore, we assessed MEM simulating varying priors in synthetic experiments with known target ensembles. We found that (i) the prior and experimental information must be carefully balanced for optimal posterior ensembles to minimize perturbations of populations by overfitting and (ii) only ensemble-integrated quantities like inter-residue distance distributions or density maps can be reliably obtained but not ensembles of atomistic structures. This is because MEM optimizes ensembles but not individual structures. This result for a highly flexible system suggests that structurally varying priors calculated from varying prior ensembles, e.g., generated with different FFs, may serve as an *ad hoc* estimate for MEM reconstruction robustness.
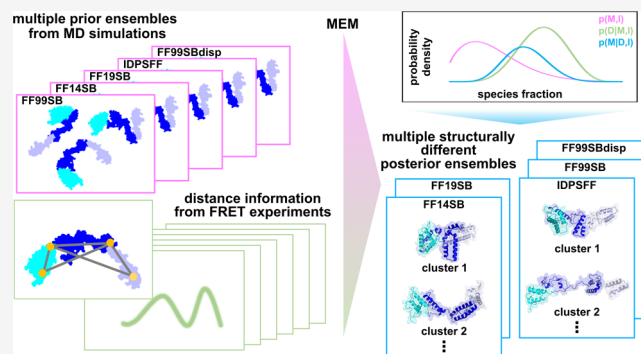

1. INTRODUCTION

To understand protein function, proteins are best described by energy landscapes, molecular ensembles, and kinetic pathways,[1] which challenges structural biology.[2] Classical experimental techniques such as X-ray crystallography, cryo-EM, or NMR can resolve fascinating snapshots of single atomistic structures. Many proteins require flexibility to function.[1,3] If the number of conformers is small and they are long-lived, the classical techniques can still resolve conformers at high resolution by varying experimental conditions.[4−7] However, multidomain proteins with unstructured segments and intrinsically disordered proteins (IDPs) are particularly challenging for structural biology due to a large number of possible conformations.[8−12] Structural ensembles were proposed for molecular systems of varying sizes and complexities, starting from small folded proteins that can be studied accurately by

NMR techniques, such as ubiquitin, for which structures and an associated dynamic model, a so-called kinetic ensemble, were reported.[13,14] Multidomain proteins with flexible linkers, such as U2AF65,[15] calmodulin,[16] or TIA-1,[17] are more challenging, as the size and associated number of degrees of freedom are substantially larger. Proteins with disorder regions, such as ESCRT complexes,[18] are even more complex, and the ultimate challenge in terms of the number of degrees of freedom is the IDPs.[19,20]
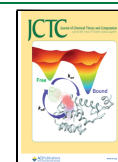
For large ensembles, no technique alone can resolve molecular ensembles in atomistic detail, as most biophysical experiments report on observables that are averages over ensembles of conformations. To overcome the limitations of individual techniques, integrative molecular modeling combines experimental information such as NMR,[15] small angle X-ray scattering (SAXS),[21] electron paramagnetic resonance (EPR),[22] Förster resonance energy transfer (FRET),[23−27] and cross-linking[28] with computational information (e.g., from molecular simulations using force fields (FFs)).[25−27,29]

Bayes theorem provides a formal framework to integrate simulated ensemble and experimental data. Combined with the maximum entropy principle, it is a suitable refinement approach for flexible systems, where no assumption about the number of states is made, as opposed to maximum-parsimony methods, where the minimum number of structures that describe experimental data is selected.[8,30] Bayes theorem expresses information in the form of probabilities, p. The theorem combines information on a model, M, experimental data, D, and prior information, I (eq 1)[31]

$$p(M|D, I) = \frac{p(D|M, I)p(M|I)}{p(D|I)} \tag{1}$$

where $p(M|D, I)$ is the posterior model density, e.g., the probability density of a conformational ensemble conditioned on D and I, $p(D|M, I)$ is the data likelihood, $p(M|I)$ is the prior model density, and $p(D|I) = Z$ is the model evidence or marginal likelihood (in analogy to statistical mechanics, $p(D|I)$ is sometimes called partition function, Z). Conformational ensembles M can be determined by restrained simulations,[32−36] where D is incorporated into the structural modeling framework.[27,37] Alternatively, $p(M|I)$ is sampled independently of $p(D|M, I)$, and $p(M|D, I)$ is computed using the independently sampled prior and likelihood. The latter approach is easy to implement, as the sampling is independent of evaluating the likelihood function. However, few sampled models might satisfy D and I either due to insufficient sampling or inaccuracies of I used for sampling (FF parameters).

Maximum entropy methods (MEMs) are statistical approaches based on Bayes' theorem that combine I, D, and M.[38] MEMs determine the maximum *a posteriori* (MAP) distribution, Q, for $p(D|M, I)$ and an entropy prior, $p(M|I)$. When MEMs are applied to recover ensembles of states for D, a set of predetermined states with corresponding population fractions is the prior information I, and the population of the states are parameters of M.[39−41] States are most commonly defined by structural similarities, and MEMs are used to optimize populations of conformers. When optimizing M, the strict convexity of the entropy prior asserts that even for underdetermined systems unique regular solutions are found.[42] However, $p(M|D, I)$ depends on I, the state distribution of the initially simulated ensemble, and D, the experimental data. Hence, both I and D impact the ensembles recovered by MEMs.

Here, we probe the robustness of MEM, i.e., the precision and accuracy, for recovering the structural diversity of the ensemble and resolving individual structures in the ensemble with respect to I, considering experimental data and its corresponding precision. For that, we determine posterior ensembles for the folding domain (FOD) of *Pseudomonas aeruginosa* lipase-specific foldase (Lif)[43,44] (Figure 1). Lif is a steric chaperone with a three-domain organization common
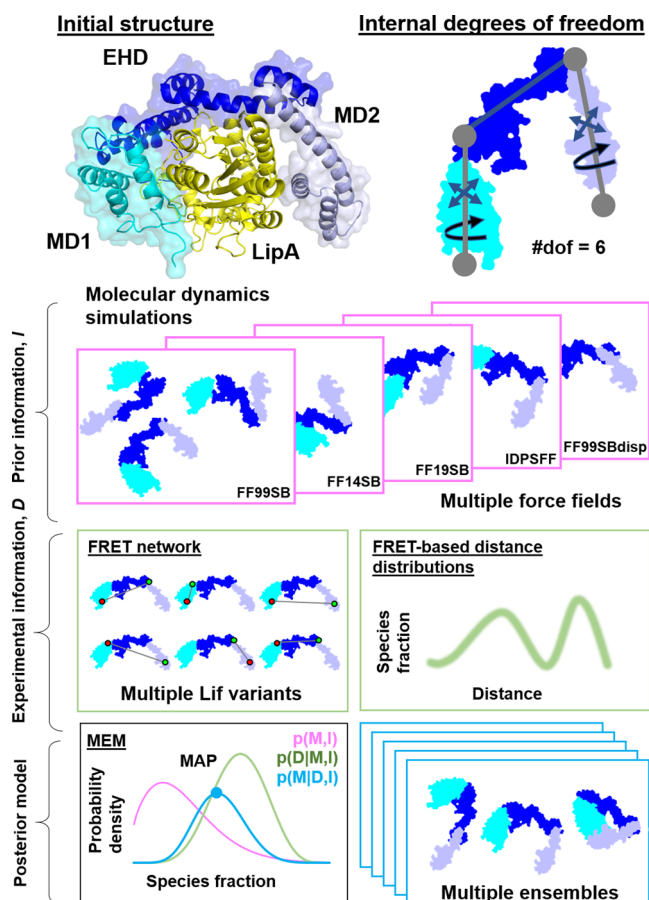

Figure 1. Maximum entropy-based ensemble refinement of lipase-specific foldase (Lif). Top left: the quaternary structure of the *P. aeruginosa* Lif:LipA complex homology model is shown, with the foldase Lif minidomains MD1 (residues 65−146, cyan), the extended helical domain EHD (residues 147−265, blue), and MD2 (residues 266−340, light blue). Lif forms a unique headphone-like fold around the lipase LipA (yellow). Top right: simplified Lif model. Three domains are assumed to act as three rigid bodies connected by two hinges (between EHD and MDs, allowing three degrees of freedom each for the MDs), yielding a model with six internal degrees of freedom. The all-atom structural information is fed into molecular dynamics simulations with five different FFs. The obtained conformational ensembles serve as a basis to calculate the interdye distance distribution in MD, i.e., the prior information I (magenta frames). FRET data acquired for the distance network provides information on interdye distance distributions D (green frames). The prior information I is combined with the FRET data D using the maximum entropy method (MEM, black frame). MEM determines the maximum a posteriori (MAP) distribution for the species fractions to produce posterior structure weights Q that represent molecular ensembles (blue frames).

with other steric chaperones.[43,45,46] Its folding domain is anchored to the inner bacterial membrane by a conserved transmembrane domain and an alanine/proline-rich flexible linker.[47] Lif activates the prefolded lipase LipA with a mechanism independent of ATP[48] by binding with the folding domain (FOD),[47] which can be divided into three subdomains: minidomains 1 and 2 (MD1, MD2), connected by the extended helical domain (EHD).[43,49] As such, Lif follows the typical architecture of multidomain proteins, where different domains of a protein are connected by linkers with different amounts of softness. The α-helical arrangement of the

EHD suggests it to be a "rigid linker" that keeps MD1 and MD2 as a molecular spacer at a certain distance.

We, therefore, geometrically approximated Lif as a 3-body object for which a small set of distance measurements should potentially resolve the domain arrangement (Figure 1) while preserving biological activity (Table S1). We used time-resolved FRET experiments and molecular dynamics (MD) simulations to acquire structural data on Lif. FRET is the distance-dependent energy migration from an excited donor fluorophore to an acceptor fluorophore;[50] time-resolved FRET experiments inform on conformational distributions with minimal conformational averaging, as snapshots of the conformers are obtained on the nanosecond time scale. Our MEM scoring uses the known single photon counting statistics (Poisson). Making use of defined data and data noise, our FRET-based MEM has a well-defined minimum that is convenient and robust for validating the consistency of the FF-dependent prior and posterior ensembles to experiments.

For integrative FRET modeling by MEM, we established the following workflow: we developed a Bayesian tool (ucFRET) that transforms time-resolved FRET data into interdye distance distributions as opposed to simple ensemble averages. For resolving conformational ensembles, we acquired data on a set of FRET experiments with a network of FRET pairs. These experiments served as experimental data, D. As input information, we used distinct conformational ensembles obtained from MD simulations with different force fields optimized for folded and unfolded proteins. To compute experimental observables as prior I for combining experimental data and computational models, we employed a forward model based on accessible volume (AV) simulations.[25,37] We optimized our prior ensembles against the FRET data and found that our priors describe the FRET data to a different extent. By varying the contribution of experimental and prior information, we searched for optimally balanced solutions (L-curve analysis).

Next, we assessed the performance of our MEM approach. We tested the effect of prioritizing experiments over the prior information to evaluate how uniquely conformations are resolved within a large ensemble at atomistic resolution and whether ensembles from distinct force fields yield similar conformers. This objective is a great challenge in general and especially for FRET because FRET mainly informs on long-range features.[37] To optimize our analysis and assess the robustness of MEM ensemble reconstructions, we performed synthetic experiments on defined conformational ensembles (target ensemble Y). We found the optimal balance for prior and experimental information that minimized the discrepancy to the target ensemble to be close to the corner of the L-curve. Using ensemble representations of varying details (atomistic representations, inter-residue distograms, and three-dimensional (3D) densities), we assessed the reliability of MEM-derived ensembles and consequences for the achieved resolution of posterior models. We found that distograms and 3D density maps are robustly recovered representations that are more appropriate to capture and identify relevant features of large and diverse posterior ensembles than individual structures. Finally, for our experimental FRET data, we find that three out of five posterior ensembles have a headphone shape as identified by the density map representation. According to the L-curve criterion, ensembles with a headphone or expanded shape are both feasible for *apo*Lif in solution.

Our results stress the need for robust uncertainty estimates of posterior ensembles. In the absence of uncertainty estimates, the distinct obtained posterior ensembles highlight the importance of using structurally varying priors to probe the robustness of MEM reconstructions.

2. MATERIALS AND METHODS

2.1. Maximum Entropy Method. MEMs used for integrative modeling are based on MaxEnt[51] methods developed for image restoration.[52] MEMs maximize the posterior model density according to eq 2

$$\arg \max_M p(M|D, I) = \arg \max_M p(D|M, I)p(M|I) \tag{2}$$

where $\arg \max_M p(M|D, I) = Q$ is the MAP distribution, i.e., the posterior model density that is maximal for M, D, and I. A set of J states defines I. In structural integrative modeling problems, a state corresponds to a conformation C_j with a prior weight $w_j^{(0)}$. Hence, $I = \{w_j^{(0)}, C_j\}_{j=1}^{j=J}$. The set of weights defines the model, $M = \{w_j\}_{j=1}^{j=J}$. Weights belong to the $J - 1$ simplex, i.e., $\sum_j w_j = 1$ and $w_j \geq 0$ for $j \in \{1, \cdots, J\}$. In MEM, $p(M|I)$ is an entropy prior (eq 3)

$$p(M|I) = \prod_{j=1}^{J} \exp(-\theta \cdot w_j \ln(w_j/w_j^{(0)})) = \exp(\theta S) \tag{3}$$

where $S = -\sum_{j=1}^{J} w_j \ln(w_j/w_j^{(0)})$ and θ is a temperature-like factor that controls the weight of the prior. $p(D|M, I) = \exp(-H)$ is the data likelihood, where H depicts the agreement of the model with D. Computing the data likelihood requires a forward model and a noise model. The forward model predicts D for M, assuming no experimental noise. The noise model quantifies the distribution of the differences between D and the forward model,[53] which originates from random experimental error, systematic experimental error, and error in the forward model; noise models generally assume that systematic and forward model errors are 0.

The forward model, the data, the noise, and the prior information affect the outcome of the modeling. In FRET experiments, the forward model requires a model of the dyes. Such dye models can compute for a given conformation the distribution of FRET rate constants. Dye models are essential parts of FRET forward models and need to be critically evaluated on a case-by-case basis. A full atomistic treatment requires separate simulations for each FRET pair as an exhaustive sampling of the dye's conformational space is challenging. We use a coarse-grained implicit dye model that was shown to be accurate. We further assume slow translational diffusion and fast rotational diffusion on the time scale of fluorescence (<4 ns). The dye model output (FRET rate constants) can be converted into time-resolved fluorescence intensities. This conversion is computationally expensive, as it requires the convolution with the instrument response function (IRF) among other experimental nuisances (e.g., background, IRF corrections, incomplete FRET labeling). Due to these nuisances, direct scoring against fluorescence decays is computationally costly. Thus, instead of approaching the modeling problem as a single-sided problem, where fluorescence decays are computed for MD simulations, we approach the modeling from two sides. First, we transform by Bayesian modeling time-resolved fluorescence intensities (and the associated data noise) into posterior model densities. We marginalize nuisance to obtain probability

densities over distance distributions. Next, for scoring of ensembles, we compute, using implicit dye models as a forward model, ensemble distance distributions. In our workflow, both the output of the Bayesian fluorescence modeling and the output of the structural forward model are distributions that abstract molecular models and experimental data, respectively. This intermediate representation allows for the computationally efficient scoring of ensembles.

In MEM, the posterior model density is defined by eq 4

$$p(M|D, I) = Z^{-1} \exp(-H + \theta S) = Z^{-1} \exp(-G) \quad (4)$$

where $G = H - \theta S$ is a free-energy-like function. For normal distributed data, $H(D, M, I) = 1/2 \cdot \chi^2$, where χ^2 is the sum of squared deviations between the forward model and the data weighted by the inverse of the noise. The maximum of $p(M|D, I)$ is obtained by solving a constrained optimization problem that maximizes $\ln(p(M|D, I))$. The MAP distribution is uniquely defined and can be determined without an expensive computation of Z^{-1} by minimizing $G = H - \theta S$ using computationally inexpensive gradient descent methods.

Here, $\{C_j\}$ and $\{w_j^{(0)}\}$ are sets of representative conformations and corresponding cluster weights from clustered MD trajectories. The initial weight $w_j^{(0)}$ of the cluster j corresponds to the fraction of that cluster within the ensemble of MD trajectories for a respective FF. The MD analysis is described in detail in a separate section.

D is a set of K FRET experiments, $D = \{D_k\}_{k=1}^{k=K}$. Each D_k measures a donor−acceptor (DA) distance, R_{DA}, distribution, $x_e(R_{DA})_k$, with the corresponding uncertainty, $\Delta x_e(R_{DA})_k$. In a forward model, for D_k, a weighted average model R_{DA} distribution, $x_m(R_{DA})_k$, is computed in two steps: first, for each D_k and entropy value, $x_m(R_{DA})_{jk}$ is computed from the accessible volume (AV) center-to-center distance,[54−56] R_{MP}, and a noncentral χ-distribution (eq 5)

$$x_m(R_{DA})_{jk} = (\sigma_{DA}\sqrt{2\pi})^{-1} \frac{R_{DA}}{R_{MP}} \left(e^{-\left(\frac{R_{DA}-R_{MP,jk}}{2\sigma_{DA}}\right)^2} - e^{-\left(\frac{R_{DA}+R_{MP,jk}}{2\sigma_{DA}}\right)^2} \right) \quad (5)$$

where σ_{DA} represents the overall broadness of $x_m(R_{DA})_{jk}$. We used $\sigma_{DA} = 8.5$ Å, as this value is consistent in reference experiments[54] and MD simulations.[57] Second, $x_m(R_{DA})_k$ is computed over all C_j using w_j as the weighting factor (eq 6)

$$x_m(R_{DA})_k = \sum_{j=1}^{J} w_j x_m(R_{DA})_{jk} \quad (6)$$

To compute χ^2, we discretize x_m and x_e into N_b bins of 1.9 Å, considering that FRET experiments are most sensitive around the Förster radius R_0. For our experiments, the reliable range is $0.65R_0-1.5R_0$.[58] For the FRET pair used here (AlexaFluor488, AlexaFluor647), $R_0 = 52$ Å; thus, the reliable range is 30−80 Å. Accordingly, distances <30 and >80 Å are represented by a single bin each. To allow for nonuniform binning, bin counts are normalized by respective bin widths. We quantify the discrepancy between M and D_k by eq 7

$$\chi_{r,k}^2 = \frac{1}{N_b}\chi_k^2 = \frac{1}{N_b} \sum_{i=1}^{N_b} \left[\frac{x_e(R_{DA}^{(i)})_k - x_m(R_{DA}^{(i)})_k}{\Delta x_e(R_{DA}^{(i)})} \right]^2 \quad (7)$$

where N_b is the total number of bins and $x_e(R_{DA}^{(i)})_k$, $x_m(R_{DA}^{(i)})_k$, and $\Delta x_e(R_{DA}^{(i)})$ are the experimental species fraction, the model species fraction, and the experimental uncertainty for the $R_{DA}^{(i)}$ bin, respectively. The overall discrepancy for all $D_k \in D$ is $\chi^2 = \sum_k \chi_k^2$. To obtain a metric less dependent on $|D| = K$, we normalize $\chi_{r,k}^2$ by the number of measurements (eq 8)

$$\chi_{r,total}^2 = \frac{1}{K} \sum_{k=1}^{K} \chi_{r,k}^2 \quad (8)$$

MEMs minimize $G = 1/2\chi_{r,total}^2 - \theta S$ by varying $\{w_j\}$.[59] We minimized G by our in-house open-source software MaxEnt-pRda (https://github.com/Fluorescence-Tools/MaxEnt-pRda). MaxEnt-pRda makes use of the Jacobian and relies on optimization algorithms provided by the scipy.optimize module. In line with others,[60] the L-BFGS-B algorithm gave the best combination of convergence speed and reliability. For the system investigated here, MaxEnt-pRda with L-BFGS-B converges in about a hundred iterations independent of the initial weights, i.e., in seconds on a current laptop.

Note that S is the negative Kullback−Leibler divergence between $w_j^{(0)}$ and the varied weight w_j. When $w_j = w_j^{(0)}$, $S = 0$. The more negative S, the less similar a posterior ensemble is to the original ensemble. The temperature-like factor θ is a separately defined hyperparameter that controls how strongly deviations between $\{w_j\}$ and $\{w_j^{(0)}\}$ are penalized. Large θ leads to small deviations of $\{w_j\}$ from $\{w_j^{(0)}\}$.[59] Small θ can cause large changes in the $\{w_j\}$ and best agreement with D but can lead to overfitting.[61] We scan θ to obtain a broad range of $\chi_{r,total}^2 - S$ pairs.

2.2. FRET Network. To acquire information on intramolecular distances by FRET experiments, we generated double cysteine variants and labeled the cysteines by AlexaFluor488-C$_5$-maleimide and AlexaFluor647-C$_2$-maleimide (Thermo Fisher Scientific) as donor and acceptor fluorophores, respectively. The set of double cysteine variants, referred to by pairs of substituted amino acid numbers, defines a network: 137−215, 137−268, 137−296, 215−268, 215−296, 255−296, 258−296, 259−296, 260−296, and 268−296. We performed ensemble time-correlated single photon counting (eTCSPC) experiments. Moreover, we performed FRET-FCS analysis[62] on data acquired on a multiparameter fluorescence detection (MFD) setup.[63,64] FCS determines a set of auto- and cross-correlation functions based on spectral channels sensitive to donor and acceptor fluorescence. The analysis of the correlation curves of FRET-labeled samples recovers relaxation times that inform us of the molecular dynamics.[62] Details on the eTCSPC and FCS analysis are provided in Supplemental Materials and Methods. The fit results are compiled in Tables S2 and S3.

2.3. Nonparametric Bayesian Analysis of eTCSPC Data (ucFRET). To maximize the precision and accuracy of recovered distance information, which serves as an input for MEM ensemble refinement and account for data noise (photon noise) ambiguities, we processed the raw eTCSPC data, D, in a Bayesian framework using the ucFRET software in four steps (i−iv). We processed the data for the FRET pairs individually and repeated the steps i−iv for all distance measurements.

In step (i), we gather all data D_l that informs us of distances between labeling sites. Here, D_l is the fluorescence decay of the FRET pair in the absence, $f_{D|D}^{(D0)}$, and presence of FRET, $f_{D|D}^{(DA)}$.

In step (ii), we define a representation suitable for D_k. The key determinant of the representation is the DA distance distribution, $x(R_{DA})_k$. We use mixture models, e.g., of Gaussian distributions, to parameterize $x(R_{DA})_k$. As a forward model to compute model fluorescence decays, we use a model for small organic fluorophores homogeneously quenched by FRET.[58] Briefly, the model factorizes $f_{D|D}^{(DA)}$ into the FRET-induced decay, $\epsilon_{D,k}(t) = \int x(R_{DA})_k \cdot e^{-k_{RET}(R_{DA})t} \, dx$, and $f_{D|D}^{(D0)}$. We use two representation types for $x(R_{DA})_k$: (a) mixtures of Gaussians of variable location, height, and width and (b) mixtures of multiple noncentral χ-distributions, χ_m (eq 5), of variable location, $R_{MP,m}$, and width, σ_{DA}; $x(R_{DA})_k = \sum_{l=1}^{L} \chi_m(R_{DA}|R_{MP,l}, \sigma_{DA})$. In representation (a), the number of Gaussians, n_G, is a hyperparameter determined by comparing scores of competing models. Typically, n_G is in the range of 1−3. In representation (b), we set the number of χ distributions, L, by the bounds of $R_{MP,m}$ and σ_{DA}. We sample σ_{DA} and $R_{MP,m}$ in the range of $[3.0 \text{ Å}, 9.0 \text{ Å}]$ and $[10 \text{ Å}, 130 \text{ Å}]$, respectively. Thus, we use $L = (130-10)/3 = 40$ as the number of χ-distributions. Representation (b) minimizes presumptions on the number of states and is better suited for systems with an undefined or large number of states. For scoring of ensembles, we used posteriors of the χ-distribution mixture models. Dyes that are normally distributed have a χ-distributed interdye distribution.

In step (iii), we optimize and sample over variable parameters and nuisance parameters of the representation to find models consistent with D_l using a scoring function that ranks models. The exact scoring function (negative log-likelihood function) considers that fluorescence decays are counting histograms with the Poisson noise as described previously.[65] We optimize representation parameters by minimizing the discrepancy between a computed model, M_k, and D_k. By minimizing the discrepancy, we obtain an M_k that best describes D_k. Moreover, we sample over variable parameters to obtain parameter probability distributions and parameter uncertainties.[27,58]

In step (iv), we analyze and interpret the optimization and sampling results. For representation (a), we obtain n_G posterior distributions of population fractions, distribution widths, and interdye distances. The population fractions inform us of the relative abundance of molecules in a state, the distribution widths of conformational heterogeneity, and the interdye distances of structural features. For representation (b), we obtain a posterior distribution over a set of separation distances, $\{R_{MP,lk}\}_{l=1}^{l=L}$, and a width σ_{DA} that relate to $p(x(R_{DA})|D_k)$, the probability of $x(R_{DA})$ conditioned on D_k. For MEM scoring, we convert $p(x(R_{DA})|D_k)$ to $p(x, R_{DA}|D_k M_k)$ (eq 9)

$$p(x, R_{DA}|D_k, M_k) = \iint \delta(R_{DA} - R'_{DA})p(x_m(R_{DA})|D_k)$$
$$dR'_{DA}dp(x_m(R_{DA})) \qquad (9)$$

and use the $p(x, R_{DA}|D_k, M_k)$ mean and standard deviation as $x_e(R_{DA})$ and $\Delta x_e(R_{DA})$ estimate, respectively, for MEM ensemble reweighting (eq 7). Assuming a fixed experimentally determined Förster radius, we sample from the posterior of the parameters using ensemble slice samplers.[66] The software implementation of the analysis framework is publicly accessible (https://hub.docker.com/r/tpeulen/ucfret).

2.4. Molecular Dynamics Simulations. All-atom MD simulations were performed for Lif using five FFs, namely,

FF99SB,[67] FF14SB,[68] FF19SB,[69] FF14IDPS[70] (here referred to as IDPSFF), and FF99SBdisp.[71] The simulations using FF99SB were performed with the Amber11 software suite[72] with the TIP3P water model,[73] and simulations using FF14SB or FF19SB were performed with Amber20.1[72] and the OPC water model.[74] Simulations using IDPSFF were performed with Amber20.1 and the recommended TIP3P water model,[70] and simulations using FF99SBdisp were performed with Amber19.4[72] and a modified version of the TIP4P-D water model, which is native to FF99SBdisp[75] (Table S4). Besides the diverse protein FFs and water models, we used different procedures for the minimization and thermalization of the systems to support generating independent structural ensembles. Details on the minimization and thermalization procedures are provided in the Supplemental Material and Methods. The SHAKE algorithm[76,77] was used in the production runs to constrain the bond lengths of hydrogen atoms, and the particle mesh Ewald method[78] was used to treat long-range electrostatic interactions with a direct-space, nonbonded cutoff of 8 Å. The integration step for the MD simulations was 2 fs. Production runs of 10 independent replicas with a length of 1 μs each were performed for all FFs. Conformations were saved at 20 ps intervals (settings collected in Table S5).

Clustering of conformations and geometrical analyses were performed with pytraj and CPPTRAJ[79] of Amber20.1.[72] To reduce the number of conformers obtained from the five sets of MD simulations, we employed hierarchical clustering using the best-fit coordinate RMSD of all atoms. We employed a maximum distance of 4 Å between the clusters as cluster criterion (average linkage) for each set of simulations. The sets of trajectories were sieved prior to clustering, i.e., the clustering was performed on every 25th frame of the trajectory set, which is equal to a time step of 0.5 ns, and the remaining frames were added to the respective clusters after the clustering. For all consecutive calculations, such as the determination of interdye distances and MEM reweighting, the pooled cluster representatives (which are the conformations closest to the cluster average) were used as $\{C_j\}$. With these settings, we obtained a total of 15,521 clusters of Lif structures. Initial cluster weights $w_j^{(0)}$ were calculated as the size of cluster j divided by the number of structures within the set of simulations. To estimate the conformational space explored by Lif, we performed a principal component analysis (PCA)[80,81] of the C_α atoms for all 15,521 cluster representatives. MEM cluster weight optimization was performed for each FF individually.

Dye positions and, therefore, donor and acceptor dye distances were estimated using the free and open-source software Olga[37] (available at https://github.com/Fluorescence-Tools/Olga).

2.5. Computation of Synthetic FRET Data. To assess the accuracy of MEM, we computed synthetic FRET data for a set of FRET pairs. In the computations, the fluorophores in a FRET pair were attached to Lif by flexible linkers with a length of 20 Å and had a Förster radius, R_0, of 52 Å. To pick the donor and acceptor attachment sites, we use a method based on an automated pair selection planning approach that selects an optimal set of FRET pairs by maximizing the information from FRET experiments as implemented in the Olga[37] software. An optimal set of FRET pairs maximizes the precision of a structural model for a given ensemble that satisfies the corresponding distance restraints. When selecting
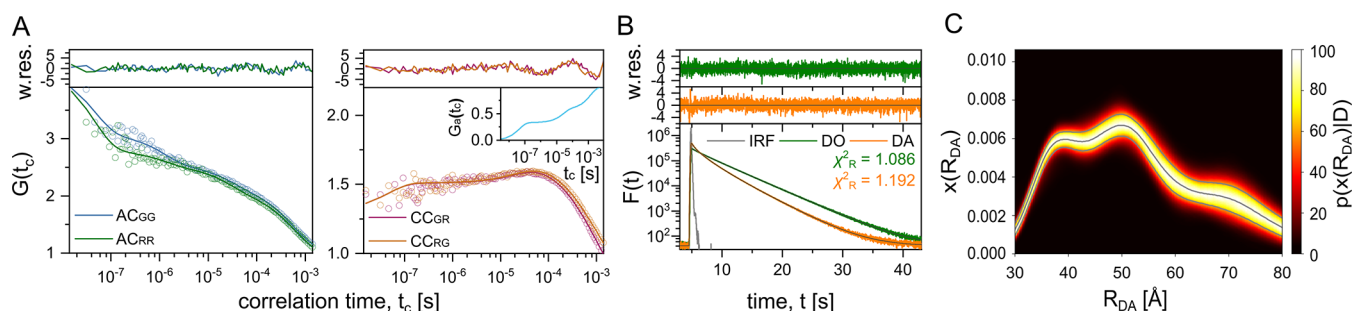
Figure 2. Fluorescence spectroscopy of Lif variant 215−296. (A) Fluorescence correlation spectroscopy (FCS). Global formal fit of the auto- (left) and cross- (right) correlation curves of donor and acceptor channels (SI eqns S1−S5). The inset in the right plot shows the donor−acceptor anticorrelation curve (SI eqn S3), indicating the presence of fast and slow Lif dynamics on the time scale reaching hundreds of microseconds. The results are compiled in Table S2. (B) Exemplary fluorescence decays measured by eTCSPC for the FRET sample (DA) and the donor-only reference sample (DO). The DO sample (green) is fitted with a multi-exponential fit with three fluorescence lifetimes τ_i and species fractions given in parentheses: 4.19 ns (0.781), 2.20 ns (0.131), 0.36 ns (0.088). The best donor−acceptor distance distribution found in Bayesian sampling for the DA sample is displayed as a fit to the orange line. The weighted residuals for the models are plotted on top. (C) Bayesian analysis of fluorescence decays. Probability of interdye distance distribution, $p(x(R_{DA})|D_k)$, conditioned on fluorescence decays of the donor in the presence and absence of the acceptor molecules. Gray lines indicate mean and 3-sigma limits of experimental model density, which are used as $x_e(R_{DA})_k$ and $\Delta x_e(R_{DA})_k$ estimates for MEM ensemble reweighting. All R_{DA} values below 30 Å and all above 80 Å are considered one additional data point each in reweighting. See Figure S4 for all other investigated Lif variants.

FRET pairs, only noncharged and polar amino acids spaced, on average, five residues apart were considered attachment sites to make a choice more experimentally plausible.

The automated FRET pair selection was run on the MD ensembles computed for individual FFs. For each of the five MD simulations for each, we obtained 30 FRET pairs. Among the 5×30 pairs, there are 120 unique FRET pairs that were used in a second step to select 50 FRET pairs that are the most informative for all FFs combined (see Supplemental Materials and Methods).

We computed fluorescence decays for an ensemble Y as previously described.[58] Briefly, for each conformer and FRET pair in a target ensemble, Y, we simulated the positional distribution of the donor and acceptor dyes around their attachment sites using the AV approach.[54] For the corresponding interdye distance distributions, we computed FRET rate constants assuming that the dyes diffuse slowly on the time scale of fluorescence. Using the homogeneous approximation that assumes uncorrelated quenching of the donor by other processes and quenching by FRET, we computed fluorescence decays of the donor in the presence of FRET.[58] The fluorescence decay of Y is the weighted average of fluorescence decays of all structures. Experimental data is perturbed by nuisances. Thus, we convolved fluorescence decays of Y with an experimental instrument response function, added nuisances such as scattered light and fluorescence of incompletely labeled molecules to the fluorescence decays, and simulated shot-noise by random draws from Poissonian distributions.[82]

2.6. Ensemble Comparison. Various representations and metrics were proposed to evaluate the similarity between conformational ensembles and determine the quality of resolved ensembles.[83−86] To assess the consistency between posterior ensembles of different FFs after FRET-MEM refinement, we used the Jensen−Shannon divergence D_{JS}[87] of residue pairwise C_α-distance histograms (distograms) and 3D density maps computed for the ensembles; the 3D density maps provide a low-resolution model representation. 3D density maps were computed by mapping coordinates of all atoms of ensemble members onto a grid of uniform dimensions (nx, ny, nz) = (100, 100, 100) and isotropic voxel size of 2 Å. Voxel occupancy of a grid corresponds to a

sum of ensemble member weights found in respective voxels. Computed 3D density maps were stored in the MRC2014 file format,[88] a standard for cryo-EM data, using the *mrcfile* python library.[89] For the precision estimate of density maps, we computed the gold-standard Fourier shell correlation (FSC) curves[90] between two independent reconstructions that are free of spurious correlations.[91,92] For that, structures of a given ensemble were split into two sets of the same size. Here, we used interleaved frames, i.e., odd and even frame numbers. For each set of frames and corresponding weights, we computed 3D density half-maps. Subsequently, FSC curves between Fourier transforms of half-maps were computed using the *EMDA* python module.[93] Finally, the precision of a full 3D density map was assigned to a point where the FSC curve crosses the threshold of 0.143.[91] All density maps were displayed using the 3D rendering program UCSF Chimera,[94] where the cross-correlation coefficient (CCC) between a pair of density maps was computed as a similarity measure between ensembles.

3. RESULTS

3.1. Prior Structural Knowledge. The *P. aeruginosa* Lif structure is unknown. However, Lif from *P. aeruginosa* and the *Burkholderia glumae* lipase-specific foldase (*Bg*Lif) have a 39% sequence identity and 52% sequence similarity. The *Bg*Lif FOD embraces its cognate lipase LipA (*Bg*LipA) to form a complex with a headphone-like structure. A homology model of *P. aeruginosa* Lif/LipA based on the *Bg*Lif/*Bg*LipA shows the same tertiary structure, with the FOD consisting of 11 α-helices connected by loops (Figure 1).[43] CD spectroscopy indicates that *Bg*Lif and *Bg*LipA undergo structural changes upon interaction.[46] Knowing that MD1 of the FOD is structurally stable[43] and assuming that MD2 and EHD are predominantly stable with the linkers in between acting as hinges in the absence of LipA, Lif can be geometrically approximated by a 3-body object with two hinge regions, having six internal degrees of freedom (Figure 1). Thus, a combination of fluorescence spectroscopy techniques and MD simulations seems well suited to characterize the conformational space of Lif.
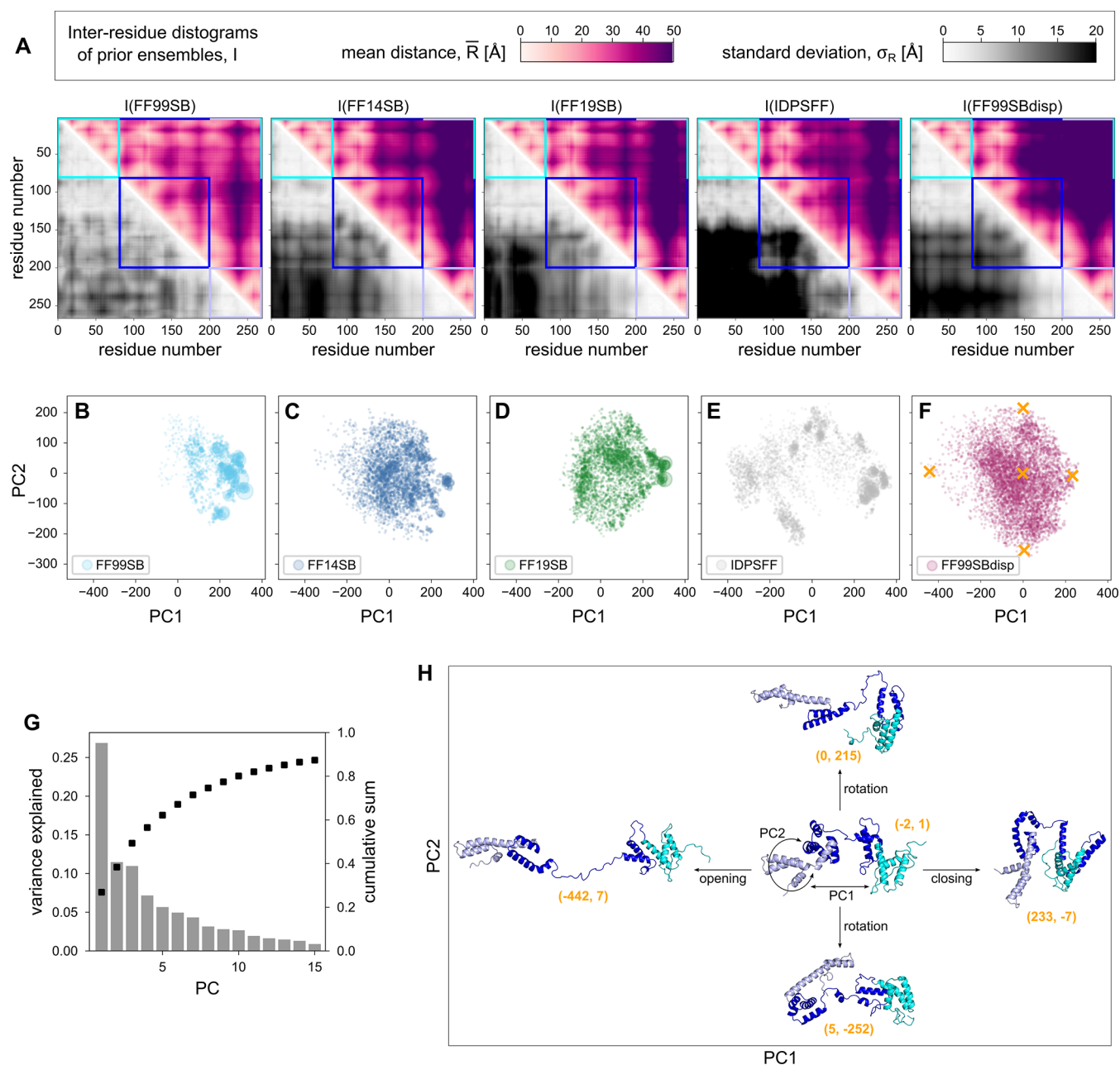
Figure 3. Distogram and principal component analysis of prior conformational ensembles. (A) Inter-residue distograms of prior Lif ensembles I obtained by MD simulations using five FFs. This representation displays the diversity of an ensemble by integrating over ensemble members while retaining the residue (sequence) information. We compute the pairwise mean, $\overline{R}$, and the standard deviation, σ_R. (B−F) Projection of C_α atom positions of cluster representatives for a given FF onto the first two principal components (PC1 and PC2) obtained from a PCA. The PCA was performed on the pooled cluster representatives of all FFs. The marker size for each representative structure scales linearly with the cluster weight. (G) Variance explained by the first 15 PCs (bars) and the cumulative explained variance (squares). (H) Representative Lif structures for different PC1/PC2 values (given in parentheses below each structure) taken from MD simulations with FF99SBdisp (orange crosses in panel F). PC1 describes the opening/closing of MD1 and MD2; PC2 describes the rotation of MD2. Lif domains are colored as in Figure 1.

3.2. Fluorescence Information. To probe the structure and dynamics of Lif, we generated a set of six double cysteine variants that define a FRET network (Figure 1). Cysteine mutations and fluorescent dyes might affect the conformations adopted by Lif. However, activity and binding assays indicate that the mutations and the fluorophores only weakly affect the ability of Lif to bind and activate LipA (Figure S1 and Table S1). We performed FRET-FCS and eTCSPC experiments on the six FRET-labeled double cysteine Lif variants. The FRET-FCS experiment provides information on time scales of exchange between conformational states; the eTCSPC experiment on a FRET sample yields information on a donor−acceptor distance distribution, $x_e(R_{DA})_k$. Our FCS data indicates that unbound Lif exhibits complex structural dynamics, covering time scales from nanoseconds to hundreds of microseconds (Figure 2A). Lif variants show various amplitudes of FRET anticorrelation, which depend on the contrast of FRET efficiencies during dynamics[62] (all curves are shown in Figure S2).

We performed eTCSPC experiments on FRET-labeled double cysteine Lif variants to obtain information on experimental interdye distance distributions $x_e(R_{DA})_k$. First, we applied the Gaussian model (eq S8) to get an insight into the inter-dye distance distribution. As an example, the fluorescence decays of Lif variant 215−296 (donor-only and donor-acceptor sample) display broad $x(R_{DA})$: $\langle R_{DA} \rangle$ = 46 Å, σ_{DA} = 16 Å. Similar features were observed for the other labeled variants (decays in Figure S3 together with fit results in Table S3). The broad $x(R_{DA})$ of *apo*Lif is a direct indication of conformational heterogeneity.[23,95,96] Since there is no indication that unbound Lif adopts discrete states, we used a Bayesian approach (ucFRET) that applies χ distributions with variable location and width (eq 5) in a mixture model to represent $x(R_{DA})$, and use $x(R_DA)$ posterior model densities (eq 9) (Figures 2B and S4) as information for later steps (Figure S5).

Our Bayesian analysis converts fluorescence decays into interdye distance distributions. We estimate the conversion precision by the posterior distribution (Figure 2C). For scoring, we use marginal distributions that do not consider correlations and underestimate the sampling precision. In addition to the precision (data noise), the model and calibration accuracy contribute to the overall uncertainty. The experiments (and simulations) were performed on dyes flexibly tethered to their host. The fluorescence of such dyes can be approximated by models where the translational dye diffusion is slow compared to the time scale of fluorescence (<4 ns).[25,54] The distance distribution between dyes normally distributed around their attachment site is χ-distributed.[97] Thus, $x(R_{DA})$ is represented by a χ distribution mixture model. Time-resolved anisotropy experiments on such dyes showed that the rotational dye diffusion is fast compared to the time scale of fluorescence. Thus, FRET rate constants can be converted to distances using a single Förster radius. Slower rotating dyes require more complex conversion schemes.[98]

3.3. Prior Conformational Ensembles from MD Simulations.

Although the FOD of Lif bound to LipA is likely structured,[43] the unbound FOD might have partially disordered regions. Thus, we performed MD simulations of the unbound FOD with five FFs optimized for folded or disordered proteins: we used standard Amber FFs optimized for folded proteins, the classic FF99SB and the more recent FF14SB as well as FF19SB, and, in addition, IDPSFF (a modified FF14SB) and FF99SBdisp that supposedly better capture features of intrinsically disordered/partially disordered proteins. We used FF99SB[67] together with the TIP3P water model in a previous study.[43] FF14SB is an updated FF99SB with improved accuracy of protein side chain and backbone parameters.[68] FF19SB is a further improvement of FF14SB, which tackles an underestimated helix stability in FF14SB.[69] IDPSFF is based on FF14SB, with the backbone dihedral terms of all 20 natural amino acids corrected for IDPs, enhancing the unfolding of collapsed proteins.[70] FF99SBdisp was reported to be capable of describing folded proteins and disordered proteins equally well. Together with its native water model,[71] FF99SBdisp applies modest changes to the backbone torsion and the strength of a backbone O−H Lennard-Jones pair potential to describe both ordered and disordered proteins accurately. For each FF, we performed 10 replicas of MD simulations of 1 μs length each. The replicas for each FF were pooled, and the conformations were clustered. The downstream analysis was performed on cluster representatives and cluster populations, i.e., cluster weights (see the Material and Methods section: clustering and geometry analyses). For FF99SB, FF14SB, FF19SB, IDPSFF, and FF99Sbdisp, we obtained 910, 3640, 2852, 2561, and 5558 clusters, respectively, for an all-atom RMSD cluster threshold of 4 Å. Surprisingly, IDPSFF, although tailored for more flexible proteins, samples more similar conformations than FF14SB and FF19SB, as indicated by the similar number of clusters. Here, we note that the cluster representatives, although capturing the conformational information within a cluster, do not necessarily conserve FRET properties in all cases due to variances in the estimation of the dye position and, therefore, interdye distances. The potential error introduced by performing the downstream analysis on cluster representatives, however, is likely to be similar for all tested FFs, as clustering was performed uniformly. To display the influence of FF on the sequence-dependent structural features of the five prior Lif ensembles, i.e., the ensembles obtained from unbiased simulations, we generate pairwise C_α inter-residue distance histograms (distograms) and show the first (mean, $\bar{R}$) and second moment (standard deviation, σ_R) (Figure 3A) revealing that MD1 (cyan box) and MD2 (light blue box) are structurally more stable in all FFs (small σ_R), while the EHD domain (blue box) is structurally variable. This has consequences for the heterogeneity of the conformational Lif ensembles, that gradually increases from FF99SB, FF19SB, FF14SB, FF99SBdisp to IDPSFF. To conclude, we obtained five different prior ensembles that cover a wide conformational space that can be tested by MEM.

Next, we further characterize the spatial domain configurations in the prior ensembles by principal component analysis to prepare the ground for a subsequent comparison of the prior I with the experimentally derived FRET data (Figure S4) by calculating interdye distance distributions for the prior ensembles (Figure S5).

We mapped the sampled conformational spaces for each FF onto the two main principal components (PCs) obtained from a PCA of the C_α atom positions of all cluster representatives (Figure 3B−F). The first two and three principal components (PCs) account for 38 and 49% of the variance, respectively (Figure 3G). The first PC (PC1) captures an opening and closing motion of Lif (Figure 3H). PC2 and PC3 capture a rotation of MD2 and MD1, respectively. We use PC1 and PC2 to highlight differences among the FFs (see Figure S6 for a projection of the first three PCs). Projection of the FF99SB-derived cluster representatives onto PC1 and PC2 covers the narrowest range of values and favors a compact conformation (Figure 3B). Both FF14SB and FF19SB sample similar conformational spaces (Figure 3A,C,D). IDPSFF samples open conformations more frequently than the other FFs; however, clusters with the highest weights are associated with compact conformations (Figure 3A,E). FF99SBdisp, by contrast, samples the PC1−PC2 space most uniformly of all FFs (Figure 3A,F).

As the stability of secondary structure elements often influences the overall rigidity and flexibility of the protein, we compare the FF's tendency to conserve structural elements such as α-helices. In all simulations, MD1 and MD2 were folded in more than 70% of the frames on average (Figure S7). Lif flexibility was dominated by the flexibility of the EHD composed of helices H4−H8. For these helices, varying secondary structure propensities dependent on the used FF were found. In MD simulations with FF14SB, FF19SB, and

FF99Sdisp, H4−H8 are predominantly helical (>70%). FF99SBdisp seemingly promotes protein flexibility (Figure 3F) while simultaneously preserving the protein's secondary structure (Figure S7). In IDPSFF and FF99SB, the Lif secondary structure is less stable (33 and 59%, respectively; Figure S7). For IDPSFF, which preserves the secondary structure of the EHD the least, this leads to broad coverage of the space spanned by the first two PCs (Figure 3E), yielding more open and closed conformations and fewer intermediate states. By contrast, for FF99SB, the partial collapse of the secondary structure of H4−H8 seemingly promotes the compaction of the protein, paralleled by the lowest number of clusters and the least coverage of the space spanned by the first two PCs (Figure 3B).

Next, we compared interdye distributions obtained from experimental data $x_e(R_{DA})_k$ with $x_m(R_{DA})_k$ based on the forward modeling of ensembles from different FFs (Figure S5). Prior ensembles describe the experimental data poorly. Overall discrepancies ($\chi^2_{r,total}$) are between 13.6 and 20.8 (Table S6). Hence, the donor−acceptor distance distributions from the simulations and experiments in general disagree. For single distances, a better agreement (minimum discrepancy, χ^2) is found for FF99SB simulations and the residue pairs 258−296 (within MD2, $\chi^2_{r,258−296}$ = 2.80) and 259−296 (within MD2, $\chi^2_{r,259−296}$ = 0.84). For other pairs, however, FF99SB simulations underestimate the distances, indicating that Lif collapsed in these simulations without consecutive unfolding or opening events (Figure S8). For FF14SB and FF19SB simulations, we find closed and open conformations. The conformational ensemble from FF19SB simulations agrees slightly better with experiments than FF14SB (Figures S9 and S10). This is particularly prominent for distances 137−215 (within MD1), 137−296 (MD1-MD2), and 137−268 (MD1-EHD). IDPSFF produced ensembles that disagree the least with the experimental data. These ensembles describe the distances 258−296 ($\chi^2_{r,258−296}$ = 2.11) similarly well as FF99SB and 137−296 slightly better ($\chi^2_{r,137−296}$ = 36.81) (Figure S11). FF99SBdisp simulations produced ensembles that agree the least with experiments. Although the FF99SBdisp ensemble describes the distances 137−215 ($\chi^2_{r,137−215}$ = 2.06) and 137−296 ($\chi^2_{r,137−296}$ = 1.15) well, it disagrees with the remaining set of distances (Figure S12). An overview of all χ^2_r for all distances and FFs is provided in Table S7. Hence, although some distances agree better with the experiments, there is no general trend that distances within a minidomain or between them stand out.

In conclusion, the chosen FFs produce structurally different ensembles, covering different regions of the combined conformational space, and show variance in secondary structure conservation. When comparing the prior I to experimental data D, we find poor agreement. Here, we note that due to the flexibility of the protein, the sampling of conformations is potentially poor for all tested FFs. Nevertheless, this approach pictures a valid real-life scenario in which a potentially poorly described prior needs to be refined using additional information.

3.4. MEM Cluster Reweighting with Experimental FRET Data.
To overcome the disagreements between MD simulations and experimental data, we used the experimental data in MEM refinement. Our FRET-FCS experiments revealed the presence of fast and slow Lif dynamics on the time scale reaching hundreds of microseconds (Figure 2A). Since the latter cannot be sufficiently sampled, we combined

experimental distance information D, with simulated distance information based on conformational ensembles from the MD simulations, the prior information I, consisting of the structure representatives of clusters and corresponding cluster weights of the MD trajectories for the different FFs. We used MEM to find conformational ensembles describing both the experimental data and the MD simulations (Figure 1) by optimizing cluster weights according to eqs 2−4 (Figure 4A). As above, we quantify the discrepancy with D using $\chi^2_{r,total}$ (eq 8). $\chi^2_{r,total} \approx$ 1 is of particular interest as ensembles with $\chi^2_{r,total}$ > 1 disagree with experimental data (under the assumptions of the used forward model). To quantify differences of prior and posterior weights of conformations, we use the entropy, S (eq 3). For $S \approx −3$, posterior ensembles from priors of FFs best describing D achieve $\chi^2_{r,total} \approx$ 1 (Figure 4B). At $S \approx −3$, the observed $\chi^2_{r,total}$ values are virtually converged for all FFs when compared to the $\chi^2_{r,total}$ values obtained at $S < −3$ (Figure 4B). Thus, we use $S \approx −3$ as a reference point for comparing posterior ensembles for different I.

In Figure 4A, we exemplarily depict initial and MEM reweighted distance distributions for the FRET pair 215−296 and FF14SB (for remaining FRET pairs and other FFs, see Figure S5). Unbiased, the ensemble has a discrepancy (eq 7) between the model and the data of $\chi^2_{(215−296)}$ (FF14SB) = 35.21. For $S = −3$, we find $\chi^2_{(215−296)}$ (FF14SB) = 0.90. The dependency of $\chi^2_{r,total}$ on S is depicted in Figure 4B for all tested FFs. For $S = −3$, $\chi^2_{r,total}$ (FF99SB) = 1.41, $\chi^2_{r,total}$ (FF14SB) = 1.16, $\chi^2_{r,total}$ (FF19SB) = 1.66, $\chi^2_{r,total}$ (IDPSFF) = 1.20, and $\chi^2_{r,total}$ (FF99SBdisp) = 1.97. To assess the significance of $\chi^2_{r,total}$ differences, the effective number of observations and the model complexity need to be considered. In a conservative significance estimate, we treat the 10 experimental distance measurements as independent and assume that only the mean, mode, skewness, and kurtosis of a distance distribution are the observed features. Moreover, we assume that Lif has six effective degrees of freedom. Thus, the total degree of freedom is 10 ×4−6 = 34, and 0.06 is an upper estimate for the p-value (F-value = 1.97/1.16 = 1.70) of the comparison of FF14SB and FF99SBdisp MEM ensembles. Consequently, the FF14SB MEM ensemble describes experiments better than the MEM FF99SBdisp. The MEM reweighting of all ensembles for all measured distances is shown in Figures S8−S12.

Overall, posterior ensembles from FF14SB and IDPSFF agree best with experimental results, yielding the lowest $\chi^2_{r,total}$ for the given entropy threshold. This result is surprising as IDPSFF was modified from FF14SB to handle intrinsically disordered proteins by enhancing the protein flexibility, which often preserves the secondary structure to a lower degree.[70] Surprisingly, FF99SBdisp, designed for both ordered and disordered proteins and which samples most uniformly the PC1−PC2 space, disagreed the most with experiments before and after MEM reweighting.

3.5. Posterior Analysis.
MEM favored a few clusters. After reweighting, the 50 clusters with the largest weights account for more than 60% of the overall weights; the top 500 clusters account for more than 95% of the overall weights (Figure 4C). For FF14SB, before applying MEM, 677 and 2790 clusters represent 60 and 95% of the conformational ensemble, respectively.

We next compared reweighted ensembles among different FFs and discussed the results for the FFs FF14SB, FF19SB, and IDPSFF because before reweighting, FF14SB and FF19SB are the most similar (Figure 3), and after reweighting, FF14SB
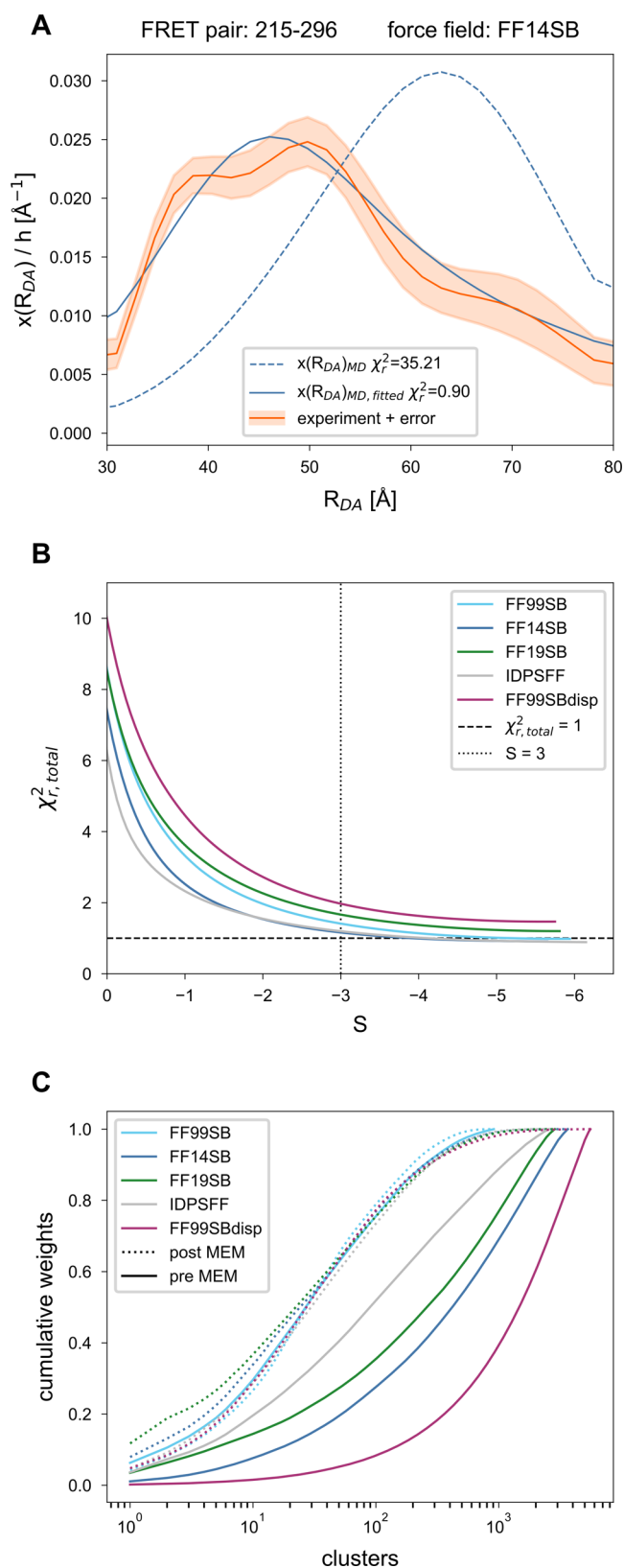
Figure 4. MEM reweighting of cluster weights increases the agreement with experiments while simultaneously reducing the number of relevant conformations. (A) R_{DA} distribution normalized by bin widths (h) for FRET pair 215−296 obtained from 10×1 μs of MD simulations using I(FF14SB) (dashed blue line) and post-MEM reweighting Q (solid blue line) in comparison to the experimental distribution of R_{DA} (orange line) and its error (orange-shaded area,

Figure 4. continued

using a confidence threshold of 0.68) obtained from ucFRET. (B) The total reduced discrepancy $\chi^2_{r,total}$ between experimental, $x_e(R_{DA})$, and model distance distributions, $x_m(R_{DA})$, versus entropy S. (C) Cumulative distribution of prior (solid lines) and posterior (dotted lines) cluster weights for five different FFs (indicated by color).

and IDPSFF ensembles described the data best and second best. The results for all remaining pairwise FF comparisons are depicted in Figures S13−S21. We compare reweighted ensembles based on two hypotheses.

First, we hypothesize that structures ranked similarly are structurally similar. To test our hypothesis, we computed all pairwise cluster representatives in terms of the C_α-RMSD and displayed these similarities for the top 50 clusters in matrices (Figure 5A,C). By definition of the cluster criterion (see above), the average C_α-RMSD of structures within a cluster differ at most by 4 Å from their representative. For FF14SB and IDPSFF, the top 50 clusters with similar weights generally have different structures (Figure 5A). The two most populated clusters (with weights of 7.9 and 5.2% (FF14SB) as well as 4.7 and 4.3% (IDPSFF)) are remarkably dissimilar: we find C_α-RMSD differences in the range of 18.1−29.3 Å (Figure 5B). For FF14SB and FF19SB, which produced comparable prior ensembles, the two most populated clusters (with weights of 7.9 and 5.2% (FF14SB) as well as 11.8 and 7.1% (FF19SB)) are remarkably dissimilar, too (Figure 5D): we find C_α-RMSD differences in the range of 11.4−20.8 Å. This result is surprising, as the conformational ensembles sampled by FF14SB and FF19SB were more similar before reweighting (C_α-RMSD differences in the range of 10.2−14.4 Å). Moreover, a visual comparison of the structures reveals different low-resolution properties such as the interdomain contacts, shapes, or radius of gyration. To conclude, we find structurally different posterior ensembles for FFs that produce posterior ensembles well describing the data (FF14SB and IDPSFF) and FFs that produce similar prior ensembles (FF14SB and FF19SB).

Furthermore, we hypothesize that clusters of high structural similarity between different posteriors have similar weights. To test our hypothesis, we compare weights of structurally similar clusters. We determined 50 cluster pairs iteratively: we selected the most similar cluster representatives between two FFs based on C_α-RMSD, discarding cluster representatives already assigned to a structure pair. The data (Figure 5E,F) reveals no correlation in the posterior weights for similar structures selected from different prior I, and this finding is independent of the magnitude of the structural similarity.

3.6. Assessment of MEM with Synthetic FRET Data. To assess which model resolution is possible from MEM reconstruction independent of the prior I, we computed synthetic FRET data. We consider the ensemble on which synthetic FRET data is computed the known target ensemble, Y. We then use Y to assess the accuracy and precision of the reconstructed posterior ensembles. We computed synthetic FRET data for two target ensembles. First, MD ensembles obtained for FF14SB depict the target ensemble, i.e., Y(FF14SB) (Figure 6A). Second, Y is a mixture of 488 structures randomly selected from a combined ensemble from MD simulations of all studied FFs, i.e., Y(all); the contribution in terms of the number of structures of each FF in target Y corresponds to the sizes of prior ensembles (FF14SB = 21.5%,
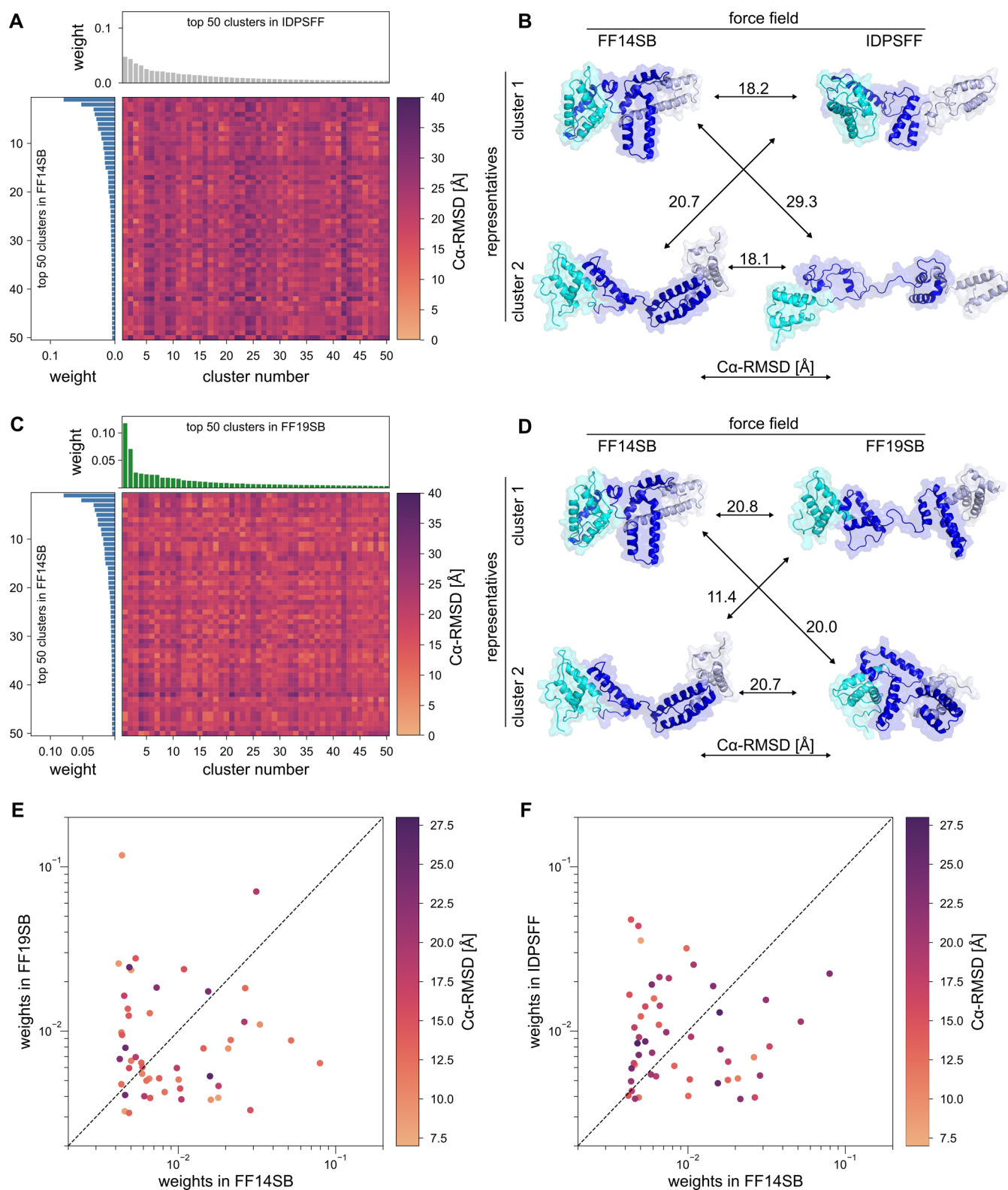
Figure 5. Comparison of posterior ensembles of FF14SB to FF19SB and IDPSFF after reweighting at an entropy threshold of $S = -3$. (A, C) C_α-RMSD matrix for the top 50 cluster representatives reveals structural dissimilarity between cluster representatives despite a reasonable agreement with experimental data in both cases ($\chi^2_{r,total}$ ($FF14SB$) = 1.16, $\chi^2_{r,total}$ ($FF19SB$) = 1.66, and $\chi^2_{r,total}$ ($IDPSFF$) = 1.20). Bar graphs depict the corresponding posterior cluster weight for the 50 most populated clusters. (B, D) Comparison of representatives of the two most populated clusters obtained from MEM. The pairwise structural similarity is given as C_α-RMSD. RMSD values in all cases exceed typical values for thermal fluctuations by 1 Å.[99] (E, F) Comparison of posterior weights of the pairwise most similar structures from the top 50 cluster representatives reveals no correlation in the posterior weights.
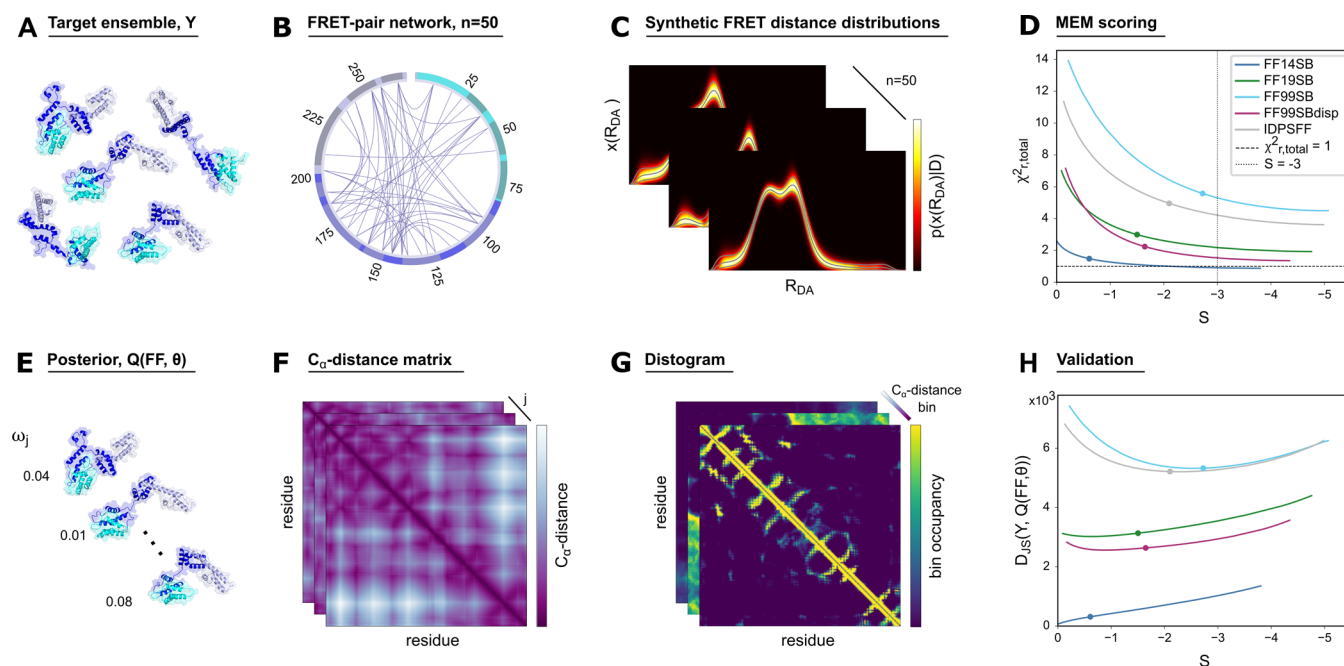
Figure 6. MEM reconstruction based on synthetic FRET data. For a given target ensemble, here Y(FF14SB) (A) and a network of the 50 most informative FRET pairs (B), we simulate fluorescence decay curves and convert them by sampling probability distributions over the population of distances (synthetic distance distribution, $x_e(R_{DA})$) (C). The total reduced discrepancy, $\chi^2_{r,total}$, between the model distance distributions, $x_m(R_{DA})$, of the posterior conformational ensemble recovered by MEM and $x_e(R_{DA})$ for all FRET network members versus the entropy, S (D). The circles mark θ_c points that balance the synthetic data D and the prior I based on the L-curve criterion. For a given posterior ensemble with structures and weights (E), we compute residue pairwise C_α-distance matrices (F) and corresponding population-weighted distograms (G). Each point in a distogram corresponds to a distance occupancy computed for C_α atoms of structures of an ensemble. To compare two ensembles, we compute the Jensen–Shannon divergence (D_{JS}) between the posterior distogram and the distogram computed for Y, here Y(FF14SB) (H).

FF19SB = 17.2%, FF99SB = 6.6%, IDPSFF = 16.4%, FF99SBdisp = 38.3%) used in the target ensemble. Uniform weights are assigned to all members of Y(all). We then selected the 50 most informative FRET pairs[37] (Figure 6B). For each FRET pair, we simulated fluorescence intensity decays for donor dyes in the presence of FRET and applied the ucFRET method to recover FRET distances (Figure 6C), which were, in turn, used to optimize the prior ensembles using MEM.

3.7. MEM Cluster Reweighting with Synthetic FRET Data. Predictably, we find that the agreement between synthetic FRET data and the posterior MEM ensembles quantified by $\chi^2_{r,total}$ improved with decreasing S (Figure 6D for Y(FF14SB), Figure S22 for Y(all), and Table S8). We quantify differences between conformational ensembles using the Jensen–Shannon divergence ($D_{JS}(Y, Q)$)[87] of the inter-residue distograms computed for the posterior ensembles, Q (Figure 6G). When refining I(FF14SB) for Y(FF14SB), $\chi^2_{r,total}$ is initially the lowest, as expected, and reaches $\chi^2_{r,total} = 1$ with the least perturbation compared to any other I (Figure 6D). Initial discrepancies between the synthetic data and the posterior ensemble for small perturbations are likely due to numerical inaccuracies, experimental noise, and systematic errors due to different forward models for structures (i.e., AV calculations) and the model used to recover experimental $x_e(R_{DA})$ (systematic errors associated with the forward model describing the fluorescence decays).[19] For Y(FF14SB) and I(FF14SB), D_{JS} continuously increases. With decreasing S, deviations between I and $Q(FF, \theta)$ are less penalized, and the synthetic FRET data is better described, which may be due to overfitting (Figures 6D and S22). In line with others,[41] for large θ, the initial ensemble remains unperturbed, and for small

θ, a few structures dominate the reweighted ensemble (Figure S23). For the other I except FF99SBdisp and FF19SB, $D_{JS}(Y, Q(FF, \theta))$ has a minimum in the proximity of the θ parameter obtained from the L-shaped curve analysis of the $\chi^2_{r,total}-S$ plot as described by Köfinger et al.[41] The proximity of the D_{JS} minimum justifies the previously used rule-of-thumb of using the "corner" of the $\chi^2_{r,total}-S$ curve[39,41,59] as a sensible choice for θ, termed θ_c; the corner is the point of maximal positive curvature.[100] In line with previous studies,[20,101] we find that when a large magnitude of S is needed to describe the experimental data, this indicates that the prior is not suited to represent the experiment. Additionally, we suggest that to compare and rank priors, one has to consider not only the initial $\chi^2_{r,total}$ but the entire evolution of the L-shaped curve, including the position of the "corner" and the reduction of the $\chi^2_{r,total}$ value at θ_c. As to FF99SBdisp and FF19SB, the L-shaped curves reveal that both priors initially fit poorly to Y(FF14SB) and require similarly strong perturbations to reach the "corner". Still, the FF99SBdisp ensemble shows a larger reduction of χ^2_r compared to FF19SB (Figure 6D).

For I(FF14SB), which matches Y(FF14SB), we found that computing the posterior using $\theta = \theta_c$ is close to the optimal reweighting as judged by the JS divergence and leads to a weaker perturbation of cumulative weights, compared to the stronger perturbation at $\theta_{S=-3}$ (Figure 7A). In C_α-RMSD matrices that compare pairwise Y to $Q(FF14SB, \theta)$, for θ_c under these ideal conditions, we find clusters with smaller C_α RMSD than for $\theta_{S=-3}$ (Figure 7B,C). The change of individual weights is considerable, however, ranging over 3 orders of magnitude and more even at optimally chosen $\theta = \theta_c$ (Figure S23). The C_α-RMSD matrices show that cluster populations
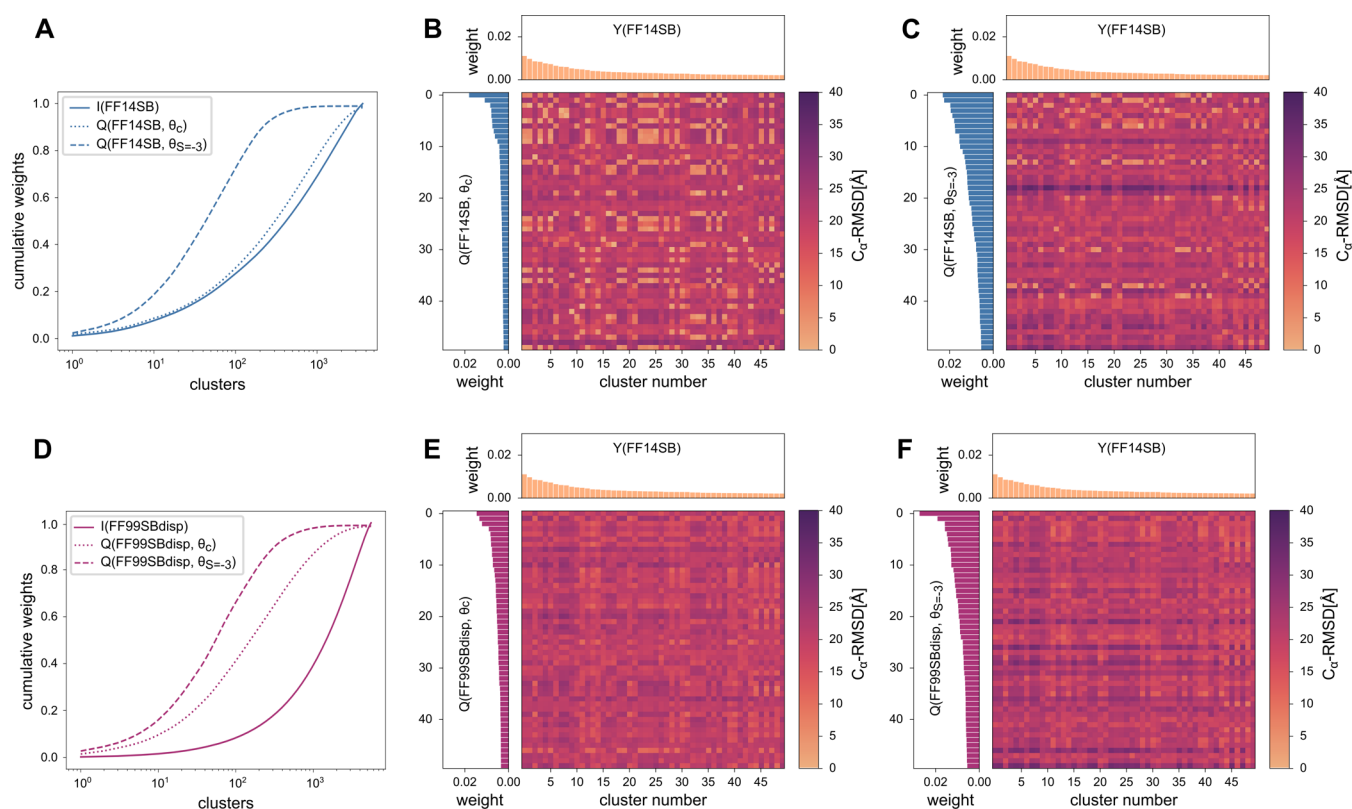
Figure 7. Cumulative weight distribution of prior I and posterior ensembles Q and pairwise $C\alpha$-RMSD matrices of the target ensemble, Y(FF14SB), and the posterior ensemble, Q, computed for θ_c and $\theta_{S=-3}$. (A) Cumulative weight for prior I(FF14SB) and posteriors Q(FF14SB, θ_c) and Q(FF14SB, $\theta_{S=-3}$). (B) Pairwise $C\alpha$-RMSD matrices of Y(FF14SB) and Q(FF14SB, θ_c) and (C) Y(FF14SB) and Q(FF14SB, $\theta_{S=-3}$). (D) Cumulative weights for I(FF99SBdisp) and Q(FF99SBdisp, θ_c) and Q(FF99SBdisp, $\theta_{S=-3}$). (E) Pairwise $C\alpha$-RMSD matrices for Y(FF14SB) and Q(FF99SBdisp, θ_c) and (F) for Y(FF14SB) and Q(FF99SBdisp, $\theta_{S=-3}$). In all panels, clusters are sorted by descending weights.

are uncorrelated to structural similarities and, therefore, indicate that individual atomistic structures of the MEM posterior have no relevance. This is expected as MEM does not optimize weights in a unique way given ensemble-average data as an experimental input.[8,9] In the case of FF99SBdisp, which is the second-best FF based on D_{JS} (Figure 6H) and provides a real-life case ($I \neq Y$), the weights are perturbed more substantially (Figures 7D and S23), and structures of Q(FF99SBdisp, θ_c) deviate by ~20 Å on average from Y (Figure 7E,F), despite using a network of 50 optimally chosen FRET pairs for the generation of D. Note that for proteins with chain lengths between 100 and 200 residues (Lif considered here has 270 residues), average C_α-RMSD values against ~2500 alternative folds taken from the PDB range from ~15 to 20 Å.[102] The average deviation between Y(FF14SB) and Q(FF99SBdisp, θ_c) found here is thus comparable to the structural dissimilarity of two randomly chosen proteins.

3.8. Robustness of Ensemble Features Resolved by MEM. In line with others,[8,9,103] we found that FRET-based MEM is not robust at providing unique solutions when individual (atomistic) structures and corresponding weights are considered. Thus, we test if there are well-resolvable ensemble features beyond the radius of gyration, a low-information ensemble feature widely used to characterize flexible molecules.[20] We compute inter-residue distograms (Figure 6F–G) as a representation for the ensemble diversity. This representation integrates over ensemble members but retains the residue (sequence) information. We compute the pairwise mean, $\bar{R}$, and the standard deviation, σ_R, and the

squared relative differences of $\bar{R}$ and σ_R ($\delta^2(\bar{R})$ and $\delta^2(\sigma_R)$ between two distograms) (Figure 8A–C). Comparing the target ensemble Y(FF14SB) with the posterior ensemble Q(FF14SB, θ_c), we find an excellent agreement between $\bar{R}$ (upper triangle) and σ_R (lower triangle) of the Y and Q distograms (Figure 8A). As expected, based on the PCA (Figure 3), the initial deviations between Y(FF14SB) and I(FF99SBdisp) are larger (Figure 8B) compared to I(FFSB14). Nevertheless, we find that MEM improves $\delta^2(\bar{R})$ 4-fold, corresponding to the improvement of the average absolute difference of $\bar{R}$, $\Delta(\bar{R})$, from 5.3 to 2.4 Å, while σ_R on average remains unchanged. For the case of Y(all) and Q(FF14SB, θ_c), $\delta^2(\bar{R})$ improves 10-fold ($\Delta(\bar{R})$ from 5.0 to 1.0 Å), while $\delta^2(\sigma_R)$ improves slightly, from 0.048 to 0.034 (Figure 8C). We find that mean distances, $\bar{R}$, are optimized overall better than σ_R. Moreover, the largest differences in $\bar{R}$ occur within EHD (dark blue frame) and between any pair of subunits, highlighting differences in the local model accuracy.

The average $\delta^2(\bar{R})$ within EHD improves 4-fold for Y(FF14SB) and Q(FF19SBdisp, θ_c) and 12-fold for Y(all) and Q(FF14SB, θ_c), corresponding to improvements of $\Delta(\bar{R})$ from 4.8 to 2.4 Å and 4.0 to 0.9 Å.

As an alternative, we characterized the structural diversity of ensembles by computing density maps of the target ensemble Y, the prior I, and the posterior Q ensembles (Figure 8D–F). Prior to the computation of density maps, target, Y, prior, I, and posterior ensemble, Q, were aligned to all atoms of the first conformer in the corresponding ensemble, which is the most populated cluster in the prior in the case of I and Q. In this
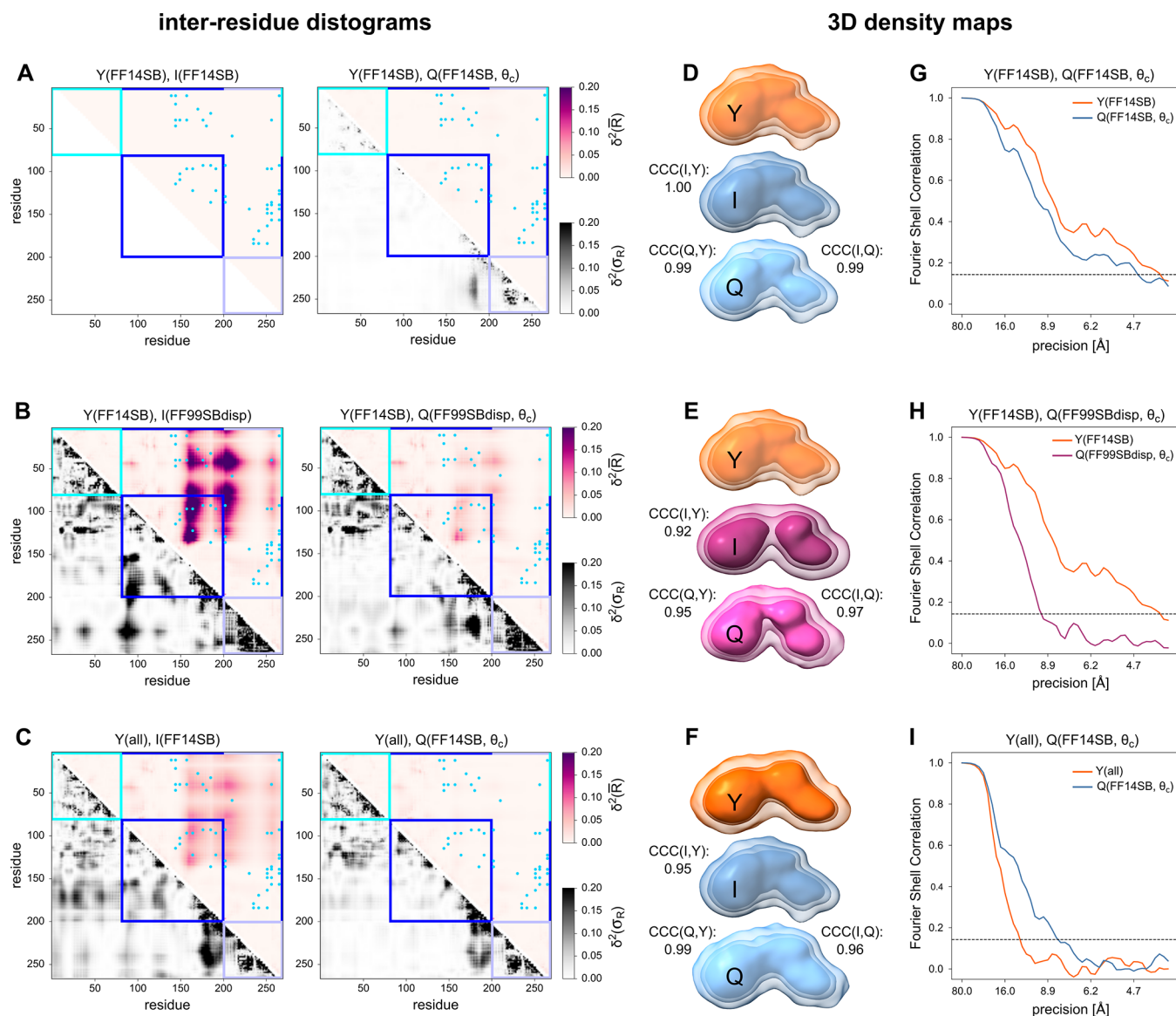
inter-residue distograms   **3D density maps**

Figure 8. Deviation of prior I and posterior ensemble Q from the target ensemble, Y, for three synthetic experiments (A−C), posterior ensemble density maps (D−F), and ensemble precision estimates (G−I). First row: case $Y = I$, a single FF is the target Y(FF14SB) and the identical FF was chosen as prior I. Second row: case $Y \neq I$, a single FF is the target Y(FF14SB) and another FF was chosen as prior I(F99SBdisp) Third row: case $Y \neq I$, a mixed ensemble from subensembles of all five FFs Y(all) and only the ensemble of one FF was chosen as prior I(FF14SB). Y(all) consists of FF14SB (fraction of 21.5% of Y), FF19SB (17.2%), FF99SB (6.6%), IDPSFF(16.4%), and FF99SBdisp (38.3%), where the fractions in terms of the number of structures of each FF in Y correspond to the sizes of prior ensembles. (A−C) Residue-wise squared relative deviation of prior (left) and posterior (right) of the distogram mean distance $\delta^2(\overline{R})$ (upper-right triangles) and standard deviation $\delta^2(\sigma_R)$ (lower-left triangles) to Y. Cyan, dark blue, and light blue squares and bars mark the residue range of the MD1, EHD, and MD2, respectively. Blue dots indicate FRET pairs. (D−F) Density maps of the target ensemble (orange), Y, the prior (FF14SB, blue; FF99SBdisp, dark pink), I, and the posterior (FF14SB, light blue; FF99SBdisp, light pink), Q, outline the extent of the experimental ensembles at 50%, 68%, and 90% of the density-weighted volume. The cross-correlation coefficients (CCCs) displayed to the left of the densities quantify similarities of prior and posterior entire density maps to the target ensemble, Y, the ones on the right similarities of prior and posterior density maps. (G−I) Fourier shell correlations (FSCs) of the two half-density maps provide precision estimates for target Y (orange) and posterior Q (FF14SB, blue; FF99SBdisp, pink) density maps. The horizontal dashed line at FSC = 0.143 marks a precision and resolution estimate for the gold standard used in electron microscopy.

model representation, we reduce the data further by averaging ensembles over clusters and residues. Representing the ensembles as density maps allows us to use the cross-correlation coefficient (CCC) of two maps as a similarity metric for two ensembles. Overall, the CCCs to the target ensemble are larger for the posterior than for the prior (Figure 8D−F; CCCs displayed to the *left* of the densities), indicating that MEM refines ensemble-integrated features. CCCs between prior and posterior are of the same magnitude,

indicating the retained structural similarity between the two despite MEM refinement. We estimated the ensemble precision of the density maps by computing Fourier shell correlation (FSC) curves of two independent half-maps (Figure 8G−I). Using an FSC threshold of 0.143, the average posterior ensemble precision is in the range of 5−10 Å. We use FSCs and CCCs to characterize ensembles and not individual structures. An ensemble with an FSC precision of 5 Å can be composed of structures that have individually a lower

Table 1. Summary of Ensemble Representations That Can Be Robustly Recovered by MEM at $\theta = \theta_c$, Depending on the Agreement between Prior and Experimental Data

completeness of prior	atomistic models[b]	distogram representation[a]		3D density map[c]
		mean	std	
prior is complete θ_c is large, i.e., small perturbation of prior weights is needed to describe the data.	−	+	+	+
prior is incomplete θ_c is small, i.e., large perturbation of prior weights is necessary, and few structures dominate the ensemble	−	+	−	+

[a]Averaging over ensemble members. [b]No averaging. [c]Structural diversity: averaging over ensemble members and residues.
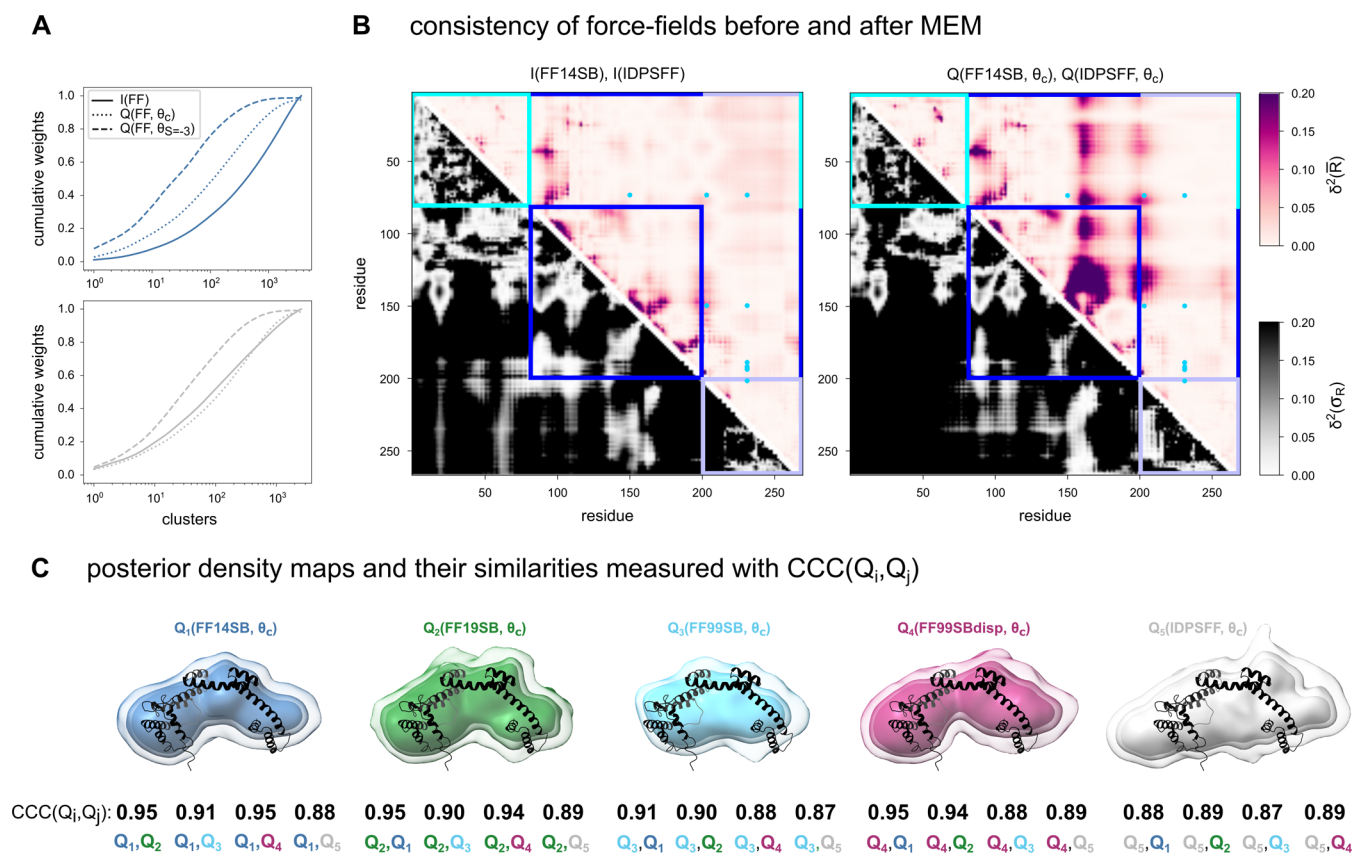

Figure 9. Experimental inter-residue distograms and posterior density maps of Lif. (A) Cumulative distributions of prior and posterior weights for FF14SB (top) and IDPSFF (bottom) ensembles reveal that smaller perturbations of prior weights occur at θ_c compared to $\theta_{S=-3}$. (B) Residue-wise squared relative deviation of distogram mean distance $\overline{R}$ and standard deviation σ_R between FF14SB and IDPSFF prior (left) and posterior (right) ensembles. (C) Posterior density maps of $Q(\text{FF}, \theta_c)$ contoured at 50, 68, and 90% of the density-weighted volume aligned to all atoms of the homology model are displayed as cartoons. Numbers below the density maps represent cross-correlation coefficient (CCC) values between the posterior density map of a respective force field to all of the others. $\text{CCC}(Q, Q)$ values are color-coded according to the force field coloring scheme.

precision. Thus, FSC ensemble precision estimates should not be compared to FSC resolution estimates of individual structures, e.g., used in cryo-electron microscopy. Moreover, note that sampling reflects the coverage of the clustered conformational ensemble. This is reflected by Y's sampling precision of ≈ 4 Å (orange curves in Figure 8G,H.) As a logical consequence, reweighting ensembles by MEM affects precision, i.e., the difference in the precision between the two FSC curves can be attributed to MEM. In the case of the mixed ensemble $Y(\text{all})$, MEM even improved the precision.

To summarize, based on the benchmark using synthetic data, we have refined our approach to optimally balance different sources of information using the L-shaped curve criterion. Furthermore, we show that to rank the priors and judge their agreement with experimental data, one should not solely rely on χ_r^2 but instead analyze the entire evolution of the L-shaped curve. We demonstrate that prioritizing one source of information over the other, i.e., relying solely on χ_r^2, leads to overfitting and increased disagreement between optimized ensembles and the ground truth (Figure 6H). In line with others, we show that, even with a network of 50 FRET pairs and in an ideal case scenario when $Y = I$, achieving atomistic resolution of the posterior ensembles is neither realistic nor feasible (Figure 7B). However, we found that representations of the ensemble diversity on a reduced level of detail (distograms and density maps) can be robustly recovered depending on the agreement between the prior and experimental data and only when optimally balancing the two sources of information by using the corner point of the L-shaped curve. An overview of which ensemble representation can be robustly recovered by MEM depending on the agreement of prior and experiments is provided in Table 1.

3.9. Reevaluation of the Experimental Data. Analyzing synthetic data for known target ensembles led us to refine our MEM approach. Therefore, we reevaluated our experimental data using low-resolution model representations of Lif obtained at the "corner" point of the L-shaped curves (Table S9). As for the synthetic data, for large θ, the prior remains unperturbed, and for small θ, a few structures tend to dominate the reweighted ensemble, which also holds at θ_c (Figure S24). This feature is prominent for FF14SB (Figure 9A, top) and also for IDPSFF, which, at θ_c, has an almost unaltered weight distribution compared to the prior, although the individual weights are perturbed as for FF14SB (Figure 9A, bottom; Figure S24). Since posterior ensembles could not be resolved in atomistic detail (Figure 5), we compare the experimentally determined posterior ensembles at an ensemble-integrated level using distograms.

Interestingly, among the FF14SB and IDPSFF ensembles that fit the experimental data best, the prior ensembles agree better in the distogram comparison than the posterior ensembles at θ_c (Figure 9B). This is in line with PCA analyses, which reveal that the conformational space of the two prior ensembles is different (Figure 3) but that this difference is exacerbated for the posteriors (Figures S25−S26). Note that the number of experimental restraints (effective 6) is much smaller than those from the synthetic data (50) and that internal conformations of EHD are not probed. In accordance, FF14SB and IDPSFF posterior distograms disagree the most for residues 150−180 of the EHD (Figure 9B). In IDPSFF, this region is unstructured in the first 20 residues, whereas it is mainly helical in FF19SB (Figure S7).

Furthermore, the similarity between density maps of FF14SB and IDPSFF ensembles is likewise not improved at θ_c compared to the priors ($CCC_{I(FF14SB,IDPSFF)}$ = 0.88, $CCC_{Q(FF14SB,IDPSFF,\theta_c)}$ = 0.88). Averaged over all FFs, we observe a slight improvement in CCCs ($\langle CCC \rangle_{I(FFs)}$ = 0.88, $\langle CCC \rangle_{Q(FFs,\theta_c)}$ = 0.91).

Based on CCCs ≥ 0.94 for all pairwise combinations of FFs (Figure 9C (bottom line); Table S10), we classified Lif density maps into three categories (Figure 9C). The first category comprises FF14SB, FF19SB, and FF99SBdisp and resembles a headphone shape; the second and third categories are, respectively, formed by FF99SB and IDPSFF, which differ equally from other FFs as from each other. The FF99SB density map represents more compact Lif, whereas the IDPSFF density map is more extended.

Overall, with our experimental data, MEM does not improve the agreement between ensemble features of different priors even at the medium-resolution level of distograms. At the low-resolution level of density maps, we obtained consistent posterior solutions for three of the five FFs. Still, the solutions with the lowest $\chi^2_{r,total}$ (FF14SB and IDPSFF) are distinct, and, at present, we cannot judge which one of the posterior ensembles, or a mixture of both, describes Lif in solution. To evaluate if further experimental data, such as SAXS measurements, could alleviate this ambiguity, we computed SAXS profiles (for details, see Supplemental Materials and Methods) of the posterior ensembles at $\theta = \theta_c$ (Figure S27). Observed differences in the predicted SAXS profiles, particularly noticeable in the Kratky plot, suggest that posterior ensembles possibly score differently against experimental SAXS data.

4. DISCUSSION

In our study, we found that in the absence of error estimation procedures, varying priors is a prerequisite for assessing the robustness of MEM results. The optimal balance between prior information and experimental data is achieved using the L-curve criterion. In view of the many degrees of freedom of the molecular system, the convergence of MEM results can only be achieved when using a distogram or 3D density map representation, depending on the consistency of priors and experimental data.

MEMs optimize posterior conformer populations by balancing information from different sources. Thus, the success of MEM ensemble refinement depends on the (i) sampling convergence and completeness of the prior, (ii) completeness of the experimental information (data sparsity), and (iii) availability of posterior uncertainty estimates. First, issues of sampling convergence and completeness of the prior ensembles can be addressed by more sampling. For *apo*Lif, we did not cover the conformational space sufficiently in 10 unbiased MD simulations with times of 1 μs each per FF, as indicated by the structural differences of the prior ensembles revealed by PCA and exchange time scales reaching hundreds of microseconds determined experimentally. More sophisticated sampling schemes, such as replica exchange simulations,[104,105] modeling transition networks,[106,107] adaptive sampling of Markov state models,[108] or machine learning-based approaches,[109] are needed. Second, the six initially chosen informative labeling site variants were insufficient to cover local conformational heterogeneity as the conformational space of the EHD was severely underestimated. To overcome data sparsity, an extension of the FRET network is necessary. However, this is related to a considerable experimental effort requiring iterative structural and biochemical analysis cycles to identify new labeling sites suitable for FRET experiments.[37] Third, another fundamental restriction is that MEMs in their current implementation lack uncertainty estimates of the posterior. MEMs yield MAP estimates given an entropy prior and the data likelihood, but these are point estimates without information on the variance. Even if MEM reconstructions ascertain that regular solutions are found for underdetermined systems, it is currently not possible to judge the robustness of the solution. Therefore, future ensemble refinement methods will need to consider varying priors, e.g., using methods such as k-fold cross-validation, Bayesian model validation, or subsampling of posterior models for estimating posterior uncertainties.[110] Overall, the presented study depicts likely challenges one might face when investigating a flexible system in an integrated approach using MEM and highlights potential pitfalls.

Previously, MEM refinement was applied to IDPs,[19,20] ordered systems,[13,59] and artificial model systems such as Ala$_5$ pentapeptide.[41] IDPs preclude a structural analysis in atomistic detail, as they are very flexible and do not adopt defined structures. Ordered systems likely can be well studied by the classical FFs, and the effective degrees of freedom of the systems that need to be covered experimentally are small. Model systems can be exhaustively sampled. Hence, in these cases, the challenges mentioned above in MEM refinement were potentially less of an issue.

Considering Lif with its ordered structural parts combined with highly flexible regions, we aimed at generating conformational ensembles for the *apo* state by combining structural

ensembles from MD simulations with FRET data using MEM. As it is not clear to what extent Lif is folded, we chose classical FFs (FF99SB, FF14SB, and FF19SB), an FF tailored to IDPs (IDPSFF), and an FF designed for ordered and disordered proteins (FF99SBdisp). This allowed assessing the recovered posterior ensemble dependency on priors and identifying inconsistencies in posteriors.

In a benchmark based on synthetic FRET data, we find that the optimal conformational ensembles are found when prior and experimental information are balanced using the L-curve criterion. Still, we were unable to obtain atomistic-level information because the ensemble and the associated conformational space are too large. MEM performed best at recovering ensemble-integrated properties (both mean and std of distograms) when the prior is complete, and only small perturbations of the ensemble are required. For cases where the prior is incomplete, e.g., due to an inaccurate FF or insufficient sampling, the recovery of these properties is less reliable, i.e., only the mean of distograms but not std and ensemble shapes are recovered. In our case study, we find that at an entropy lower than our estimated corner of the L-shaped curve ($S = -3$), also medium-resolution features (means of distograms) diverged more from the target ensemble despite lower χ_r^2, indicating overfitting. Hence, we recommend not relying solely on the agreement with experimental data (χ_r^2) but instead to balance sources of information with the L-corner criterion. Thus, scoring by MEM is convenient and robust for validating the overall consistency of the FF-dependent prior and posterior ensembles to experiments because the minimum of the quality parameter, χ_r^2, is well-known and defined and overfitting can be controlled by the L-corner criterium.

Similarly, when using experimental data, the posterior ensembles differ structurally, also for FFs that produce posterior ensembles that best describe the data (FF14SB and IDPSFF) or FFs that produce similar prior ensembles (FF14SB and FF19SB). Likewise, no correlation between the posterior cluster weights was found for similar structures selected from different prior ensembles, independent of the magnitude of the structural similarity. No consistency between posteriors was found for ensemble-integrated features such as distograms either. Only when considering posterior density maps as low-resolution information, MEM yields three distinct outcomes for the five priors. Three posteriors suggest that despite the tendency of Lif to adopt compact and extended conformations, "headphone"-like extended conformations dominate the conformational landscape, reflecting that Lif consists of ordered structural parts combined with highly flexible regions.

In line with others,[9,61,111] we conclude that using cluster-resolved, atomistic-level representations for MEM with ensemble-averaged experimental observables is an ill-defined problem. Accordingly, for this, we obtained multiple different ensembles that depend on their prior. Going to medium- and low-resolution model representations (means of distograms and density maps), we obtain partially consistent results based on different priors, making the problem well defined. Furthermore, our results caution against the interpretation of MEM reconstructions for such heterogeneous systems as studied here when single-point estimates of conformational ensembles are interpreted without additional uncertainty estimates. Using structurally varying priors, e.g., generated with different FFs, is an *ad hoc* approach to estimating the robustness of MEM reconstructions.

■ ASSOCIATED CONTENT

ⓢ Supporting Information

The Supporting Information is available free of charge at https://pubs.acs.org/doi/10.1021/acs.jctc.2c01090.

■ AUTHOR INFORMATION

Corresponding Authors

Karl-Erich Jaeger − *Institute of Molecular Enzyme Technology, Heinrich Heine University Düsseldorf, 40225 Düsseldorf, Germany; Institute of Bio- and Geosciences (IBG-1: Biotechnology), Forschungszentrum Jülich GmbH, 52425 Jülich, Germany*; Phone: (+49) 2461 613716; Email: k.-e.jaeger@fz-juelich.de

Claus A. M. Seidel − *Institute for Molecular Physical Chemistry, Heinrich Heine University Düsseldorf, 40225 Düsseldorf, Germany*; ⓞ orcid.org/0000-0002-5171-149X; Phone: (+49) 211 81 15881; Email: cseidel@hhu.de

Thomas-Otavio Peulen − *Department of Bioengineering and Therapeutic Sciences and Department of Pharmaceutical Chemistry and Quantitative Biosciences Institute (QBI), University of California, San Francisco, San Francisco 94143 California, United States of America*; Phone: (+49) 211 81 15881; Email: thomas.otavio.peulen@gmail.com

Holger Gohlke − *Institute for Pharmaceutical and Medicinal Chemistry, Heinrich Heine University Düsseldorf, 40225 Düsseldorf, Germany; John von Neumann Institute for Computing (NIC), Jülich Supercomputing Centre (JSC), and Institute of Bio- and Geosciences (IBG-4: Bioinformatics), Forschungszentrum Jülich GmbH, 52425 Jülich, Germany*; ⓞ orcid.org/0000-0001-8613-1447; Phone: (+49) 211 81 13662; Email: gohlke@uni-duesseldorf.de; Fax: (+49) 211 81 13847

Authors

Jonas Dittrich − *Institute for Pharmaceutical and Medicinal Chemistry, Heinrich Heine University Düsseldorf, 40225 Düsseldorf, Germany*; ⓞ orcid.org/0000-0003-2377-2268

Milana Popara − *Institute for Molecular Physical Chemistry, Heinrich Heine University Düsseldorf, 40225 Düsseldorf, Germany*; ⓞ orcid.org/0000-0003-2626-6096

Jakub Kubiak − *Institute for Molecular Physical Chemistry, Heinrich Heine University Düsseldorf, 40225 Düsseldorf, Germany*

Mykola Dimura − *Institute for Molecular Physical Chemistry, Heinrich Heine University Düsseldorf, 40225 Düsseldorf, Germany*

Bastian Schepers − *Institute for Pharmaceutical and Medicinal Chemistry, Heinrich Heine University Düsseldorf, 40225 Düsseldorf, Germany*

Neha Verma − *Institute for Pharmaceutical and Medicinal Chemistry, Heinrich Heine University Düsseldorf, 40225 Düsseldorf, Germany*

Birte Schmitz − *Institute for Pharmaceutical and Medicinal Chemistry, Heinrich Heine University Düsseldorf, 40225 Düsseldorf, Germany*

Peter Dollinger − *Institute of Molecular Enzyme Technology, Heinrich Heine University Düsseldorf, 40225 Düsseldorf, Germany*

Filip Kovacic − *Institute of Molecular Enzyme Technology, Heinrich Heine University Düsseldorf, 40225 Düsseldorf, Germany*

Complete contact information is available at:
https://pubs.acs.org/10.1021/acs.jctc.2c01090

Author Contributions

[∇]J.D. and M.P. contributed equally.

Author Contributions

J.D.: investigation, formal analysis, visualization, and writing—original draft; M.P.: investigation, formal analysis, visualization, and writing—review and editing; J.K.: investigation, fluorescence measurements, experimental data analysis, visualization, and writing—review and editing; M.D.: software-MEM implementation; Ba.S., N.V., and Bi.S.: investigation; P.D.: sample preparation and LipA activity measurements; F.K. and K.-E.J.: project administration and funding acquisition; C.A.M.S.: conceptualization, writing—review and editing, project administration, and funding acquisition; T.-O.P.: investigation, software-ucFRET, design of analysis, formal analysis, and writing—original draft; H.G.: conceptualization, writing—review and editing, project administration, and funding acquisition.

Funding

Notes

The authors declare no competing financial interest.

■ ACKNOWLEDGMENTS

■ REFERENCES

(1) Henzler-Wildman, K.; Kern, D. Dynamic personalities of proteins. *Nature* 2007, 450, 964−972.

(2) Kern, D. From structure to mechanism: skiing the energy landscape. *Nat. Methods* 2021, 18, 435−436.

(3) Smock, R. G.; Gierasch, L. M. Sending Signals Dynamically. *Science* 2009, 324, 198−203.

(4) Dashti, A.; Mashayekhi, G.; Shekhar, M.; Ben Hail, D.; Salah, S.; Schwander, P.; des Georges, A.; Singharoy, A.; Frank, J.; Ourmazd, A. Retrieving functional pathways of biomolecules from single-particle snapshots. *Nat. Commun.* 2020, 11, 4734.

(5) Neudecker, P.; Robustelli, P.; Cavalli, A.; Walsh, P.; Lundström, P.; Zarrine-Afsar, A.; Sharpe, S.; Vendruscolo, M.; Kay, L. E. Structure of an Intermediate State in Protein Folding and Aggregation. *Science* 2012, 336, 362−366.

(6) Kato, H.; van Ingen, H.; Zhou, B.-R.; Feng, H.; Bustin, M.; Kay, L. E.; Bai, Y. Architecture of the high mobility group nucleosomal protein 2-nucleosome complex as revealed by methyl-based NMR. *Proc. Natl. Acad. Sci. U.S.A.* 2011, 108, 12283−12288.

(7) Bertram, K.; Agafonov, D. E.; Liu, W.-T.; Dybkov, O.; Will, C. L.; Hartmuth, K.; Urlaub, H.; Kastner, B.; Stark, H.; Lührmann, R. Cryo-EM structure of a human spliceosome activated for step 2 of splicing. *Nature* 2017, 542, 318−323.

(8) Thomasen, F. E.; Lindorff-Larsen, K. Conformational ensembles of intrinsically disordered proteins and flexible multidomain proteins. *Biochem. Soc. Trans.* 2022, 50, 541−554.

(9) Bonomi, M.; Heller, G. T.; Camilloni, C.; Vendruscolo, M. Principles of protein structural ensemble determination. *Curr. Opin. Struct. Biol.* 2017, 42, 106−116.

(10) Kruschel, D.; Zagrovic, B. Conformational averaging in structural biology: issues, challenges and computational solutions. *Mol. Biosyst.* 2009, 5, 1606−1616.

(11) Borgia, A.; Borgia, M. B.; Bugge, K.; Kissling, V. M.; Heidarsson, P. O.; Fernandes, C. B.; Sottini, A.; Soranno, A.; Buholzer, K. J.; Nettels, D.; Kragelund, B. B.; Best, R. B.; Schuler, B. Extreme disorder in an ultrahigh-affinity protein complex. *Nature* 2018, 555, 61−66.

(12) Tompa, P. On the supertertiary structure of proteins. *Nat. Chem. Biol.* 2012, 8, 597−600.

(13) Lindorff-Larsen, K.; Best, R. B.; DePristo, M. A.; Dobson, C. M.; Vendruscolo, M. Simultaneous determination of protein structure and dynamics. *Nature* 2005, 433, 128−132.

(14) Smith, C. A.; Mazur, A.; Rout, A. K.; Becker, S.; Lee, D.; de Groot, B. L.; Griesinger, C. Enhancing NMR derived ensembles with kinetics on multiple timescales. *J. Biomol. NMR* 2020, 74, 27−43.

(15) Huang, J.-r.; Warner, L. R.; Sanchez, C.; Gabel, F.; Madl, T.; Mackereth, C. D.; Sattler, M.; Blackledge, M. Transient Electrostatic Interactions Dominate the Conformational Equilibrium Sampled by Multidomain Splicing Factor U2AF65: A Combined NMR and SAXS Study. *J. Am. Chem. Soc.* 2014, 136, 7068−7076.

(16) Bertini, I.; Gupta, Y. K.; Luchinat, C.; Parigi, G.; Peana, M.; Sgheri, L.; Yuan, J. Paramagnetism-Based NMR Restraints Provide Maximum Allowed Probabilities for the Different Conformations of Partially Independent Protein Domains. *J. Am. Chem. Soc.* 2007, 129, 12786−12794.

(17) Larsen, A. H.; Wang, Y.; Bottaro, S.; Grudinin, S.; Arleth, L.; Lindorff-Larsen, K. Combining molecular dynamics simulations with small-angle X-ray and neutron scattering data to study multi-domain proteins in solution. *PLoS Comput. Biol.* 2020, 16, e1007870.

(18) Boura, E.; Różycki, B.; Herrick, D. Z.; Chung, H. S.; Vecer, J.; Eaton, W. A.; Cafiso, D. S.; Hummer, G.; Hurley, J. H. Solution structure of the ESCRT-I complex by small-angle X-ray scattering, EPR, and FRET spectroscopy. *Proc. Natl. Acad. Sci. U.S.A.* 2011, 108, 9437−9442.

(19) Crehuet, R.; Buigues, P. J.; Salvatella, X.; Lindorff-Larsen, K. Bayesian-Maximum-Entropy Reweighting of IDP Ensembles Based on NMR Chemical Shifts. *Entropy* 2019, 21, 898.

(20) Hermann, M. R.; Hub, J. S. SAXS-Restrained Ensemble Simulations of Intrinsically Disordered Proteins with Commitment to the Principle of Maximum Entropy. *J. Chem. Theory Comput.* 2019, 15, 5103−5115.

(21) Kikhney, A. G.; Svergun, D. I. A practical guide to small angle X-ray scattering (SAXS) of flexible and intrinsically disordered proteins. *FEBS Lett.* 2015, 589, 2570−2577.

(22) Weickert, S.; Cattani, J.; Drescher, M. Intrinsically Disordered Proteins (IDPs) Studied by EPR and in-cell EPR. In *Electron Paramagnetic Resonance*; The Royal Society of Chemistry, 2019; Vol. 26, pp 1−37.

(23) Haas, E.; Wilchek, M.; Katchalski-Katzir, E.; Steinberg, I. Z. Distribution of end-to-end distances of oligopeptides in solution as estimated by energy transfer. *Proc. Natl. Acad. Sci. U.S.A.* 1975, 72, 1807−1811.

(24) Lerner, E.; Barth, A.; Hendrix, J.; Ambrose, B.; Birkedal, V.; Blanchard, S. C.; Börner, R.; Sung Chung, H.; Cordes, T.; Craggs, T.

D.; Deniz, A. A.; Diao, J.; Fei, J.; Gonzalez, R. L.; Gopich, I. V.; Ha, T.; Hanke, C. A.; Haran, G.; Hatzakis, N. S.; Hohng, S.; Hong, S.-C.; Hugel, T.; Ingargiola, A.; Joo, C.; Kapanidis, A. N.; Kim, H. D.; Laurence, T.; Lee, N. K.; Lee, T.-H.; Lemke, E. A.; Margeat, E.; Michaelis, J.; Michalet, X.; Myong, S.; Nettels, D.; Peulen, T.-O.; Ploetz, E.; Razvag, Y.; Robb, N. C.; Schuler, B.; Soleimaninejad, H.; Tang, C.; Vafabakhsh, R.; Lamb, D. C.; Seidel, C. A. M.; Weiss, S. FRET-based dynamic structural biology: Challenges, perspectives and an appeal for open-science practices. *eLife* **2021**, *10*, e60416.

(25) Kalinin, S.; Peulen, T.; Sindbert, S.; Rothwell, P. J.; Berger, S.; Restle, T.; Goody, R. S.; Gohlke, H.; Seidel, C. A A toolkit and benchmark study for FRET-restrained high-precision structural modeling. *Nat. Methods* **2012**, *9*, 1218–25.

(26) Dimura, M.; Peulen, T. O.; Hanke, C. A.; Prakash, A.; Gohlke, H.; Seidel, C. A. M. Quantitative FRET studies and integrative modeling unravel the structure and dynamics of biomolecular systems. *Curr. Opin. Struct. Biol.* **2016**, *40*, 163–185.

(27) Sanabria, H.; Rodnin, D.; Hemmen, K.; Peulen, T.-O.; Felekyan, S.; Fleissner, M. R.; Dimura, M.; Koberling, F.; Kühnemuth, R.; Hubbell, W.; Gohlke, H.; Seidel, C. A. M. Resolving dynamics and function of transient states in single enzyme molecules. *Nat. Commun.* **2020**, *11*, 1231.

(28) Molnar, K. S.; Bonomi, M.; Pellarin, R.; Clinthorne, G. D.; Gonzalez, G.; Goldberg, S. D.; Goulian, M.; Sali, A.; DeGrado, W. F. Cys-Scanning Disulfide Crosslinking and Bayesian Modeling Probe the Transmembrane Signaling Mechanism of the Histidine Kinase, PhoQ. *Structure* **2014**, *22*, 1239–1251.

(29) Furtmann, F.; Porta, N.; Hoang, D. T.; Reiners, J.; Schumacher, J.; Gottstein, J.; Gohlke, H.; Smits, S. H. J. Characterization of the nucleotide-binding domain NsrF from the BceAB-type ABC-transporter NsrFP from the human pathogen Streptococcus agalactiae. *Sci. Rep.* **2020**, *10*, 15208.

(30) Ravera, E.; Sgheri, L.; Parigi, G.; Luchinat, C. A critical assessment of methods to recover information from averaged data. *Phys. Chem. Chem. Phys.* **2016**, *18*, 5686–5701.

(31) Jaynes, E. T. The Relation of Bayesian and Maximum Entropy Methods. In *Maximum-Entropy and Bayesian Methods in Science and Engineering*; Springer, 1988; pp 25–29.

(32) Robustelli, P.; Kohlhoff, K.; Cavalli, A.; Vendruscolo, M. Using NMR Chemical Shifts as Structural Restraints in Molecular Dynamics Simulations of Proteins. *Structure* **2010**, *18*, 923–933.

(33) Sinelnikova, A.; Spoel, D. v. d. NMR refinement and peptide folding using the GROMACS software. *J. Biomol. NMR* **2021**, *75*, 143–149.

(34) Pitera, J. W.; Chodera, J. D. On the Use of Experimental Observations to Bias Simulated Ensembles. *J. Chem. Theory Comput.* **2012**, *8*, 3445–3451.

(35) Marinelli, F.; Faraldo-Gómez, J. D. Ensemble-Biased Metadynamics: A Molecular Simulation Method to Sample Experimental Distributions. *Biophys. J.* **2015**, *108*, 2779–2782.

(36) White, A. D.; Dama, J. F.; Voth, G. A. Designing Free Energy Surfaces That Match Experimental Data with Metadynamics. *J. Chem. Theory Comput.* **2015**, *11*, 2451–2460.

(37) Dimura, M.; Peulen, T.-O.; Sanabria, H.; Rodnin, D.; Hemmen, K.; Hanke, C. A.; Seidel, C. A. M.; Gohlke, H. Automated and optimally FRET-assisted structural modeling. *Nat. Commun.* **2020**, *11*, 5394.

(38) Shannon, C. E. A mathematical theory of communication. *Bell Syst. Tech. J.* **1948**, *27*, 379–423.

(39) Bottaro, S.; Bengtsen, T.; Lindorff-Larsen, K. Integrating Molecular Simulation and Experimental Data: A Bayesian/Maximum Entropy Reweighting Approach. In *Structural Bioinformatics*; Springer, 2020; pp 219–240.

(40) Boomsma, W.; Ferkinghoff-Borg, J.; Lindorff-Larsen, K. Combining Experiments and Simulations Using the Maximum Entropy Principle. *PLoS Comput. Biol.* **2014**, *10*, e1003406.

(41) Köfinger, J.; Stelzl, L. S.; Reuter, K.; Allande, C.; Reichel, K.; Hummer, G. Efficient Ensemble Refinement by Reweighting. *J. Chem. Theory Comput.* **2019**, *15*, 3390–3401.

(42) De Martino, A.; De Martino, D. An introduction to the maximum entropy approach and its application to inference problems in biology. *Heliyon* **2018**, *4*, e00596.

(43) Viegas, A.; Dollinger, P.; Verma, N.; Kubiak, J.; Viennet, T.; Seidel, C. A. M.; Gohlke, H.; Etzkorn, M.; Kovacic, F.; Jaeger, K.-E. Structural and dynamic insights revealing how lipase binding domain MD1 of *Pseudomonas aeruginosa* foldase affects lipase activation. *Sci. Rep.* **2020**, *10*, 3578.

(44) Rosenau, F.; Tommassen, J.; Jaeger, K.-E. Lipase-Specific Foldases. *ChemBioChem* **2004**, *5*, 152–161.

(45) Pauwels, K.; Van Molle, I.; Tommassen, J.; Van Gelder, P. Chaperoning Anfinsen: the steric foldases. *Mol. Microbiol.* **2007**, *64*, 917–922.

(46) El Khattabi, M.; Van Gelder, P.; Bitter, W.; Tommassen, J. Role of the Lipase-specific Foldase of *Burkholderia glumae* as a Steric Chaperone. *J. Biol. Chem.* **2000**, *275*, 26885–26891.

(47) Frenken, L. G. J.; de Groot, A.; Tommassen, J.; Verrips, C. T. Role of the lipB gene product in the folding of the secreted lipase of *Pseudomonas glumae*. *Mol. Microbiol.* **1993**, *9*, 591–599.

(48) Ellis, R. J. Steric chaperones. *Trends Biochem. Sci* **1998**, *23*, 43–45.

(49) Pauwels, K.; Lustig, A.; Wyns, L.; Tommassen, J.; Savvides, S. N.; Van Gelder, P. Structure of a membrane-based steric chaperone in complex with its lipase substrate. *Nat. Struct. Mol. Biol.* **2006**, *13*, 374–375.

(50) Förster, T. Zwischenmolekulare Energiewanderung und Fluoreszenz. *Ann. Phys.* **1948**, *437*, 55–75.

(51) Jaynes, E. T. Information Theory and Statistical Mechanics. *Phys. Rev.* **1957**, *106*, 620–630.

(52) Skilling, J. The Axioms of Maximum Entropy. In *Maximum-Entropy and Bayesian Methods in Science and Engineering*; Springer, 1988; pp 173–187.

(53) Schneidman-Duhovny, D.; Pellarin, R.; Sali, A. Uncertainty in integrative structural modeling. *Curr. Opin. Struct. Biol.* **2014**, *28*, 96–104.

(54) Sindbert, S.; Kalinin, S.; Nguyen, H.; Kienzler, A.; Clima, L.; Bannwarth, W.; Appel, B.; Müller, S.; Seidel, C. A. M. Accurate Distance Determination of Nucleic Acids via Förster Resonance Energy Transfer: Implications of Dye Linker Length and Rigidity. *J. Am. Chem. Soc.* **2011**, *133*, 2463–2480.

(55) Klose, D.; Holla, A.; Gmeiner, C.; Nettels, D.; Ritsch, I.; Bross, N.; Yulikov, M.; Allain, F. H. T.; Schuler, B.; Jeschke, G. Resolving distance variations by single-molecule FRET and EPR spectroscopy using rotamer libraries. *Biophys. J.* **2021**, *120*, 4842–4858.

(56) Hellenkamp, B.; Schmid, S.; Doroshenko, O.; Opanasyuk, O.; Kühnemuth, R.; Rezaei Adariani, S.; Ambrose, B.; Aznauryan, M.; Barth, A.; Birkedal, V.; Bowen, M. E.; Chen, H.; Cordes, T.; Eilert, T.; Fijen, C.; Gebhardt, C.; Götz, M.; Gouridis, G.; Gratton, E.; Ha, T.; Hao, P.; Hanke, C. A.; Hartmann, A.; Hendrix, J.; Hildebrandt, L. L.; Hirschfeld, V.; Hohlbein, J.; Hua, B.; Hübner, C. G.; Kallis, E.; Kapanidis, A. N.; Kim, J.-Y.; Krainer, G.; Lamb, D. C.; Lee, N. K.; Lemke, E. A.; Levesque, B.; Levitus, M.; McCann, J. J.; Naredi-Rainer, N.; Nettels, D.; Ngo, T.; Qiu, R.; Robb, N. C.; Röcker, C.; Sanabria, H.; Schlierf, M.; Schröder, T.; Schuler, B.; Seidel, H.; Streit, L.; Thurn, J.; Tinnefeld, P.; Tyagi, S.; Vandenberk, N.; Vera, A. M.; Weninger, K. R.; Wünsch, B.; Yanez-Orozco, I. S.; Michaelis, J.; Seidel, C. A. M.; Craggs, T. D.; Hugel, T. Precision and accuracy of single-molecule FRET measurements—a multi-laboratory benchmark study. *Nat. Methods* **2018**, *15*, 669–676.

(57) Gansen, A.; Valeri, A.; Hauger, F.; Felekyan, S.; Kalinin, S.; Tóth, K.; Langowski, J.; Seidel, C. A. M. Nucleosome disassembly intermediates characterized by single-molecule FRET. *Proc. Natl. Acad. Sci. U.S.A.* **2009**, *106*, 15308–15313.

(58) Peulen, T.-O.; Opanasyuk, O.; Seidel, C. A. M. Combining Graphical and Analytical Methods with Molecular Simulations To Analyze Time-Resolved FRET Measurements of Labeled Macromolecules Accurately. *J. Phys. Chem. B* **2017**, *121*, 8211–8241.

(59) Różycki, B.; Kim, Y. C.; Hummer, G. SAXS Ensemble Refinement of ESCRT-III CHMP3 Conformational Transitions. *Structure* **2011**, *19*, 109−116.

(60) Orioli, S.; Larsen, A. H.; Bottaro, S.; Lindorff-Larsen, K. How to learn from inconsistencies: Integrating molecular simulations with experimental data. In *Progress in Molecular Biology and Translational Science*; Strodel, B.; Barz, B., Eds.; Academic Press, 2020; Chapter 3, Vol. *170*, pp 123−176.

(61) Hummer, G.; Köfinger, J. Bayesian ensemble refinement by replica simulations and reweighting. *J. Chem. Phys.* **2015**, *143*, 243150.

(62) Felekyan, S.; Sanabria, H.; Kalinin, S.; Kuhnemuth, R.; Seidel, C. A. M. Analyzing Forster Resonance Energy Transfer with Fluctuation Algorithms. *Fluorescence Fluctuation Spectroscopy (Ffs), Pt B* **2013**, *519*, 39−85.

(63) Sisamakis, E.; Valeri, A.; Kalinin, S.; Rothwell, P. J.; Seidel, C. A. M.Accurate Single-Molecule Fret Studies Using Multiparameter Fluorescence Detection. In *Methods in Enzymology*; Academic Press, 2010; Vol. *475*, pp 455−514.

(64) Kudryavtsev, V.; Sikor, M.; Kalinin, S.; Mokranjac, D.; Seidel, C. A. M.; Lamb, D. C. Combining MFD and PIE for Accurate Single-Pair Forster Resonance Energy Transfer Measurements. *ChemPhysChem* **2012**, *13*, 1060−1078.

(65) Maus, M.; Cotlet, M.; Hofkens, J.; Gensch, T.; De Schryver, F. C.; Schaffer, J.; Seidel, C. A. M. An Experimental Comparison of the Maximum Likelihood Estimation and Nonlinear Least-Squares Fluorescence Lifetime Analysis of Single Molecules. *Anal. Chem.* **2001**, *73*, 2078−2086.

(66) Karamanis, M.; Beutler, F. Ensemble slice sampling. *Stat. Comput.* **2021**, *31*, 61.

(67) Hornak, V.; Abel, R.; Okur, A.; Strockbine, B.; Roitberg, A.; Simmerling, C. Comparison of multiple Amber force fields and development of improved protein backbone parameters. *Proteins: Struct., Funct., Bioinf.* **2006**, *65*, 712−725.

(68) Maier, J. A.; Martinez, C.; Kasavajhala, K.; Wickstrom, L.; Hauser, K. E.; Simmerling, C. ff14SB: Improving the Accuracy of Protein Side Chain and Backbone Parameters from ff99SB. *J. Chem. Theory Comput.* **2015**, *11*, 3696−3713.

(69) Tian, C.; Kasavajhala, K.; Belfon, K. A. A.; Raguette, L.; Huang, H.; Migues, A. N.; Bickel, J.; Wang, Y.; Pincay, J.; Wu, Q.; Simmerling, C. ff19SB: Amino-Acid-Specific Protein Backbone Parameters Trained against Quantum Mechanics Energy Surfaces in Solution. *J. Chem. Theory Comput.* **2020**, *16*, 528−552.

(70) Song, D.; Luo, R.; Chen, H.-F. The IDP-Specific Force Field ff14IDPSFF Improves the Conformer Sampling of Intrinsically Disordered Proteins. *J. Chem. Inf. Model.* **2017**, *57*, 1166−1178.

(71) Robustelli, P.; Piana, S.; Shaw, D. E. Developing a molecular dynamics force field for both folded and disordered protein states. *Proc. Natl. Acad. Sci. U.S.A.* **2018**, *115*, E4758−E4766.

(72) Case, D. A.; Ben-Shalom, I. Y.; Brozell, S. R.; Cerutti, D. S.; Cheatham, T. E., III; Cruzeiro, V. W. D.; Darden, T. A.; Duke, R. E.; Ghoreishi, D.; Gilson, M. K.; Gohlke, H.; Goetz, A. W.; Greene, D.; Harris, R.; Homeyer, N.; Izadi, S.; Kovalenko, A.; Kurtzman, T.; Lee, T. S.; LeGrand, S.; Li, P.; Lin, C.; Liu, J.; Luchko, T.; Luo, R.; Mermelstein, D. J.; Merz, K. M.; Miao, Y.; Monard, G.; Nguyen, C.; Nguyen, H.; Omelyan, I.; Onufriev, A.; Pan, F.; Qi, R.; Roe, D. R.; Roitberg, A.; Sagui, C.; Schott-Verdugo, S.; Shen, J.; Simmerling, C. L.; Smith, J.; Salomon-Ferrer, R.; Swails, J.; Walker, R. C.; Wang, J.; Wei, H.; Wolf, R. M.; Wu, X.; Xiao, L.; York, D. M.; Kollman, P. A. *AMBER*; University of California: San Francisco, 2021.

(73) Jorgensen, W. L.; Chandrasekhar, J.; Madura, J. D.; Impey, R. W.; Klein, M. L. Comparison of simple potential functions for simulating liquid water. *J. Chem. Phys.* **1983**, *79*, 926−935.

(74) Izadi, S.; Anandakrishnan, R.; Onufriev, A. V. Building Water Models: A Different Approach. *J. Phys. Chem. Lett.* **2014**, *5*, 3863−3871.

(75) Gopal, S. M.; Wingbermühle, S.; Schnatwinkel, J.; Juber, S.; Herrmann, C.; Schäfer, L. V. Conformational Preferences of an Intrinsically Disordered Protein Domain: A Case Study for Modern Force Fields. *J. Phys. Chem. B* **2021**, *125*, 24−35.

(76) Hammonds, K. D.; Ryckaert, J.-P. On the convergence of the SHAKE algorithm. *Comput. Phys. Commun.* **1991**, *62*, 336−351.

(77) Ryckaert, J.-P.; Ciccotti, G.; Berendsen, H. J. C. Numerical integration of the cartesian equations of motion of a system with constraints: molecular dynamics of n-alkanes. *J. Comput. Phys.* **1977**, *23*, 327−341.

(78) Darden, T.; York, D.; Pedersen, L. Particle mesh Ewald: An N·log(N) method for Ewald sums in large systems. *J. Chem. Phys.* **1993**, *98*, 10089−10092.

(79) Roe, D. R.; Cheatham, T. E. PTRAJ and CPPTRAJ: Software for Processing and Analysis of Molecular Dynamics Trajectory Data. *J. Chem. Theory Comput.* **2013**, *9*, 3084−3095.

(80) Galindo-Murillo, R.; Roe, D. R.; Cheatham, T. E. On the absence of intrahelical DNA dynamics on the μs to ms timescale. *Nat. Commun.* **2014**, *5*, 5152.

(81) Galindo-Murillo, R.; Roe, D. R.; Cheatham, T. E. Convergence and reproducibility in molecular dynamics simulations of the DNA duplex d(GCACGAACGAACGAACGC). *Biochim. Biophys. Acta, Gen. Subj.* **2015**, *1850*, 1041−1058.

(82) Becker, W. *The bh TCSPC Handbook*, 9th ed.; Becker & Hickl GmbH, 2021.

(83) Yang, S.; Salmon, L.; Al-Hashimi, H. M. Measuring similarity between dynamic ensembles of biomolecules. *Nat. Methods* **2014**, *11*, 552−554.

(84) Tiberti, M.; Papaleo, E.; Bengtsen, T.; Boomsma, W.; Lindorff-Larsen, K. ENCORE: Software for Quantitative Ensemble Comparison. *PLoS Comput. Biol.* **2015**, *11*, e1004415.

(85) Lindorff-Larsen, K.; Ferkinghoff-Borg, J. Similarity Measures for Protein Ensembles. *PLoS One* **2009**, *4*, e4203.

(86) McClendon, C. L.; Hua, L.; Barreiro, G.; Jacobson, M. P. Comparing Conformational Ensembles Using the Kullback−Leibler Divergence Expansion. *J. Chem. Theory Comput.* **2012**, *8*, 2115−2126.

(87) Lin, J. Divergence measures based on the Shannon entropy. *IEEE Trans. Inf. Theory* **1991**, *37*, 145−151.

(88) Cheng, A.; Henderson, R.; Mastronarde, D.; Ludtke, S. J.; Schoenmakers, R. H. M.; Short, J.; Marabini, R.; Dallakyan, S.; Agard, D.; Winn, M. MRC2014: Extensions to the MRC format header for electron cryo-microscopy and tomography. *J. Struct. Biol.* **2015**, *192*, 146−150.

(89) Burnley, T.; Palmer, C. M.; Winn, M. Recent developments in the CCP-EM software suite. *Acta Crystallogr., Sect. D: Struct. Biol.* **2017**, *73*, 469−477.

(90) Henderson, R.; Sali, A.; Baker, M. L.; Carragher, B.; Devkota, B.; Downing, K. H.; Egelman, E. H.; Feng, Z.; Frank, J.; Grigorieff, N.; Jiang, W.; Ludtke, S. J.; Medalia, O.; Penczek, P. A.; Rosenthal, P. B.; Rossmann, M. G.; Schmid, M. F.; Schröder, G. F.; Steven, A. C.; Stokes, D. L.; Westbrook, J. D.; Wriggers, W.; Yang, H.; Young, J.; Berman, H. M.; Chiu, W.; Kleywegt, G. J.; Lawson, C. L. Outcome of the First Electron Microscopy Validation Task Force Meeting. *Structure* **2012**, *20*, 205−214.

(91) Rosenthal, P. B.; Henderson, R. Optimal Determination of Particle Orientation, Absolute Hand, and Contrast Loss in Single-particle Electron Cryomicroscopy. *J. Mol. Biol.* **2003**, *333*, 721−745.

(92) Scheres, S. H. W.; Chen, S. Prevention of overfitting in cryo-EM structure determination. *Nat. Methods* **2012**, *9*, 853−854.

(93) Warshamanage, R.; Yamashita, K.; Murshudov, G. N. EMDA: A Python package for Electron Microscopy Data Analysis. *J. Struct. Biol.* **2022**, *214*, 107826.

(94) Pettersen, E. F.; Goddard, T. D.; Huang, C. C.; Couch, G. S.; Greenblatt, D. M.; Meng, E. C.; Ferrin, T. E. UCSF Chimera—A visualization system for exploratory research and analysis. *J. Comput. Chem.* **2004**, *25*, 1605−1612.

(95) Lakowicz, J. R.; Gryczynski, I.; Wiczk, W.; Laczko, G.; Prendergast, F. C.; Johnson, M. L. Conformational distributions of melittin in water / methanol mixtures from frequency-domain measurements of nonradiative energy transfer. *Biophys. Chem.* **1990**, *36*, 99−115.

(96) Lakowicz, J. R.; Gryczynski, I.; Laczko, G.; Wiczk, W.; Johnson, M. L. Distribution of distances between the tryptophan and the N-

terminal residue of melittin in its complex with calmodulin, troponin C, and phospholipids. *Protein Sci.* **1994**, *3*, 628−637.

(97) Barth, A.; Opanasyuk, O.; Peulen, T.-O.; Felekyan, S.; Kalinin, S.; Sanabria, H.; Seidel, C. A. M. Unraveling multi-state molecular dynamics in single-molecule FRET experiments. I. Theory of FRET-lines. *J. Chem. Phys.* **2022**, *156*, 141501.

(98) Hummer, G.; Szabo, A. Dynamics of the Orientational Factor in Fluorescence Resonance Energy Transfer. *J. Phys. Chem. B* **2017**, *121*, 3331−3339.

(99) Zaccai, G. How Soft Is a Protein? A Protein Dynamics Force Constant Measured by Neutron Scattering. *Science* **2000**, *288*, 1604−1607.

(100) Hansen, P. C.; O'Leary, D. P. The Use of the L-Curve in the Regularization of Discrete Ill-Posed Problems. *SIAM J. Sci. Comput.* **1993**, *14*, 1487−1503.

(101) Rangan, R.; Bonomi, M.; Heller, G. T.; Cesari, A.; Bussi, G.; Vendruscolo, M. Determination of Structural Ensembles of Proteins: Restraining vs Reweighting. *J. Chem. Theory Comput.* **2018**, *14*, 6632−6641.

(102) Reva, B. A.; Finkelstein, A. V.; Skolnick, J. What is the probability of a chance prediction of a protein structure with an rmsd of 6 å? *Fold Des.* **1998**, *3*, 141−147.

(103) Gomes, G.-N. W.; Namini, A.; Gradinaru, C. C. Integrative Conformational Ensembles of Sic1 Using Different Initial Pools and Optimization Methods. *Front. Mol. Biosci.* **2022**, *9*, 910956.

(104) Hansmann, U. H. E. Parallel tempering algorithm for conformational studies of biological molecules. *Chem. Phys. Lett.* **1997**, *281*, 140−150.

(105) Sugita, Y.; Okamoto, Y. Replica-exchange molecular dynamics method for protein folding. *Chem. Phys. Lett.* **1999**, *314*, 141−151.

(106) Noé, F.; Fischer, S. Transition networks for modeling the kinetics of conformational change in macromolecules. *Curr. Opin. Struct. Biol.* **2008**, *18*, 154−162.

(107) Noé, F.; Krachtus, D.; Smith, J. C.; Fischer, S. Transition Networks for the Comprehensive Characterization of Complex Conformational Change in Proteins. *J. Chem. Theory Comput.* **2006**, *2*, 840−857.

(108) Bowman, G. R.; Ensign, D. L.; Pande, V. S. Enhanced Modeling via Network Theory: Adaptive Sampling of Markov State Models. *J. Chem. Theory Comput.* **2010**, *6*, 787−794.

(109) Noé, F.; De Fabritiis, G.; Clementi, C. Machine learning for protein folding and dynamics. *Curr. Opin. Struct. Biol.* **2020**, *60*, 77−84.

(110) Lele, S. R. How Should We Quantify Uncertainty in Statistical Inference? *Front. Ecol. Evol.* **2020**, *8*, 35.

(111) Rieping, W.; Habeck, M.; Nilges, M. Inferential Structure Determination. *Science* **2005**, *309*, 303−306.

📖 Recommended by ACS

Circuit Topology Approach for the Comparative Analysis of Intrinsically Disordered Proteins

Barbara Scalvini, Alireza Mashaghi, *et al.*

APRIL 07, 2023
JOURNAL OF CHEMICAL INFORMATION AND MODELING   READ 🗗

Free Energy Differences from Molecular Simulations: Exact Confidence Intervals from Transition Counts

Pavel Kříž, Vojtěch Spiwok, *et al.*

MARCH 16, 2023
JOURNAL OF CHEMICAL THEORY AND COMPUTATION   READ 🗗

Active Learning of the Conformational Ensemble of Proteins Using Maximum Entropy VAMPNets

Diego E. Kleiman and Diwakar Shukla

APRIL 07, 2023
JOURNAL OF CHEMICAL THEORY AND COMPUTATION   READ 🗗

Learning Correlations between Internal Coordinates to Improve 3D Cartesian Coordinates for Proteins

Jie Li, Teresa Head-Gordon, *et al.*

FEBRUARY 07, 2023
JOURNAL OF CHEMICAL THEORY AND COMPUTATION   READ 🗗

Get More Suggestions >